Multitarget, selective compound design yields picomolar inhibitors of a kinetoplastid pteridine reductase 1

Ina Pöhner[1,2†], Antonio Quotadamo[3,4†], Joanna Panecka-Hofman[1,5], Rosaria Luciani[6], Matteo Santucci[6], Pasquale Linciano[6], Giacomo Landi[7], Flavio Di Pisa[7], Lucia Dello Iacono[7], Cecilia Pozzi[7], Stefano Mangani[7], Sheraz Gul[8], Gesa Witt[8], Bernhard Ellinger[8], Maria Kuzikov[8], Nuno Santarem[9], Anabela Cordeiro-da-Silva[9,10], Maria Paola Costi[6*], Alberto Venturelli[3*] and Rebecca C. Wade[1,2,11,12*]

1. Molecular and Cellular Modeling Group, Heidelberg Institute for Theoretical Studies (HITS), D-69118 Heidelberg, Germany.
2. Faculty of Biosciences, Heidelberg University, D-69120 Heidelberg, Germany.
3. Tydock Pharma srl, Strada Gherbella 294/B, 41126 Modena, Italy.
4. Clinical and Experimental Medicine PhD Program, University of Modena and Reggio Emilia, 41121 Modena, Italy.
5. Faculty of Physics, University of Warsaw, 02-093 Warsaw, Poland.
6. Department of Life Sciences, University of Modena and Reggio Emilia, Via Campi 103, 41125 Modena, Italy.
7. Department of Biotechnology, Chemistry and Pharmacy, University of Siena, 53100 Siena, Italy.
8. Fraunhofer-IME ScreeningPort, Schnackenburgallee 114, D-22525 Hamburg, Germany.
9. Instituto de Investigação e Inovação em Saúde, Institute for Molecular and Cell Biology, Universidade do Porto, 4200-135 Porto, Portugal.
10. Faculty of Pharmacy, University of Porto, 4050-313 Porto, Portugal.
11. Center for Molecular Biology (ZMBH), DKFZ-ZMBH Alliance, Heidelberg University, D-69120 Heidelberg, Germany
12. Interdisciplinary Center for Scientific Computing (IWR), Heidelberg University, D-69120 Heidelberg, Germany.

Abstract

The optimization of compounds with multiple targets in the drug discovery cycle is a difficult multidimensional problem. Here, we present a systematic, multidisciplinary approach to the development of selective anti-parasitic compounds. Efficient microwave-assisted synthesis of pteridines along with iterations of crystallographic structure determination were used to validate computational docking predictions and support derivation of a structure-activity relationship for multitarget inhibition. This approach yielded compounds showing picomolar inhibition of *T. brucei* pteridine reductase 1 (PTR1), nanomolar inhibition of *L. major* PTR1, along with selective submicromolar inhibition of parasitic dihydrofolate reductase (DHFR). Moreover, by combining design for polypharmacology with a property-based on-parasite optimization, we found three compounds that exhibited micromolar EC_{50} values against *T. brucei brucei*, whilst retaining their target inhibition. Our results provide a basis for the further development of pteridine-based compounds and we expect our multitarget approach to be generally applicable to the design and optimization of anti-infective agents.

Keywords

Kinetoplastid; antiparasitic inhibitors; folate pathway enzymes; structure-based drug design; virtual screening; microwave assisted organic synthesis; structure-activity relationships; polypharmacology

Introduction

The World Health Organization has identified 17 Neglected Tropical Diseases (NTDs) that pose a health burden to over 1.4 billion of people.[1,2] Parasites of the Trypanosomatid family are responsible for two potentially lethal insect-vector borne NTDs: Human African Trypanosomiasis (HAT, sleeping sickness), caused by *Trypanosoma brucei*, and

leishmaniasis, caused by the intracellular parasite *Leishmania spp.*[3-7] Current therapeutics are limited by toxicity, poor efficacy and parasite resistance, thus underlining the need for new chemotherapies.[8,9]

One way to identify new anti-parasitic agents is to apply target-based drug design strategies.[10-12] The folate pathway enzyme dihydrofolate reductase (DHFR) is a known anti-cancer, anti-bacterial and anti-malarial target.[13-16] It provides reduced folates, which are crucial to biological processes like DNA, protein and amino acid synthesis or one-carbon transfer.[14,17,18] In Trypanosomatids, DHFR inhibition was found to be ineffective due to a metabolic bypass via the biopterin-reducing pteridine reductase 1 (PTR1, Figure **1**): When DHFR is inhibited, PTR1, which can also reduce folates, is overexpressed and sustains sufficient metabolite levels to ensure parasite survival. Thus, when targeting the folate pathway in *Leishmania*, both DHFR and PTR1 need to be considered.[19-21] In *T. brucei*, PTR1 was shown to be a potential anti-parasitic target in its own right by RNA interference studies.[22,23] Nonetheless, even nanomolar PTR1 inhibitors have so far shown limited anti-parasitic activity *in vitro*[24,25], suggesting that targeting the *T. brucei* folate pathway may also benefit from the consideration of both PTR1 and DHFR.

Screening a set of folate-related compounds against parasitic folate pathway targets previously led to the identification of compounds **6a** (methyl-1-(4-(((2,4-diaminopteridin-6-yl)methyl)amino)benzoyl)piperidine-4-carboxylate, herein compound **2**) and **6b** (methyl-1-(4-(((2,4-diaminopteridin-6-yl) methyl) (methyl) amino) benzoyl) piperidine-4-carboxylate, herein compound **1**) as submicromolar inhibitors of *Leishmania major* PTR1 (*Lm*PTR1) with K_i values of 0.10 µM and 0.04 µM, respectively.[26] **2** was additionally a micromolar inhibitor of *L. major* DHFR (*Lm*DHFR) with a weak selectivity for the parasite enzyme over the human DHFR (hDHFR) (K_i of 4 µM vs. 10 µM). In contrast to the parasite DHFR, which is covalently coupled with thymidylate synthase (TS) in a bifunctional DHFR-TS, the hDHFR off-target is monofunctional and shares only about 30% sequence identity with parasite DHFR domains, indicating potential for further selectivity optimization.[27-29]

The aim of the current work was to optimize pteridine-based compounds for their inhibition of *T. brucei* PTR1 (*Tb*PTR1) and *Tb*DHFR, in addition to the *Leishmania* targets, while ensuring selectivity against the off-target hDHFR. The enzymatic evaluation of reference pteridines reported earlier[26,30] and our published comparative study of trypanosomatid folate pathway proteins[31] supported the design of three series of compounds to explore substituents at three positions on the pteridine structure, and a fourth 'merged' series containing permutations of the substituents in the three series. Docking simulations and three new crystallographic complexes of pteridines with *Tb*PTR1 and a complex with *Lm*PTR1, supported the target-based design approach and the determination of structure-activity relationships. A systematic analysis of correlations between computed physicochemical molecular descriptors and

observed anti-parasitic effects allowed us to prioritize promising compounds for synthesis. In total, 26 new pteridine derivatives were characterized experimentally, most of which showed improved target inhibitory profiles for PTR1 and DHFR of both *L. major* and *T. brucei*. Among these, we report the first, to the best of our knowledge, picomolar inhibitors of *Tb*PTR1 and several new low nanomolar inhibitors of *Lm*PTR1, which mostly also show selective micromolar to submicromolar inhibition of the parasite DHFR variants. *In vitro* evaluations of the effect on *T. brucei brucei* bloodstream forms revealed three new inhibitors with low micromolar to submicromolar EC_{50} values against the *T. brucei* parasite.

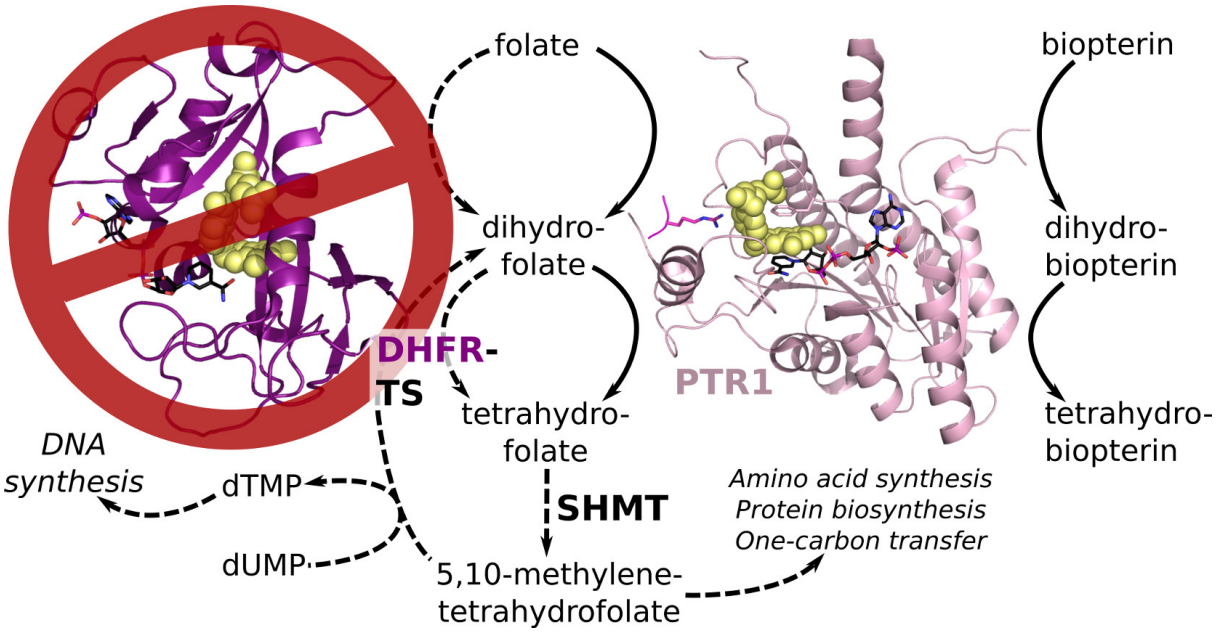

Figure 1. Overview of the pterin activation in the Trypanosomatidic folate pathway when DHFR is inhibited and PTR1 provides a metabolic bypass. The DHFR domain of the bifunctional DHFR-TS would, under normal conditions, reduce biological folates to tetrahydrofolate (THF). THF is converted to 5,10-methylene THF by the serine hydroxymethyl transferase (SHMT) and this metabolite has a central role in amino acid synthesis, protein biosynthesis and one-carbon transfer. It is also required by the TS domain of DHFR-TS to convert deoxyuridine monophosphate (dUMP) to deoxythymidine monophosphate (dTMP), which is necessary for DNA synthesis. PTR1, which primarily reduces unconjugated pterins like biopterin, takes over folate reduction when DHFR is inhibited, thus acting as a metabolic bypass and an important additional target that needs to be inhibited for shutting down the Trypanosomatidic folate pathway. Both proteins are shown in cartoon representation (DHFR domain of DHFR-TS: purple, PTR1: light pink, single monomer of functional tetramer) with the NADPH/$NADP^+$ cofactor in sticks with black carbons and the folate substrate in yellow spheres. In PTR1, in addition, an arginine residue from a neighboring subunit pointing into the active site is shown in magenta sticks.

Results

Reference compounds inhibit both PTR1 and DHFR and adopt a methotrexate-like binding mode

To systematically assess multitarget inhibition, we measured the inhibition of *Tb*PTR1, *Tb*DHFR, *Lm*PTR1, *Lm*DHFR, and the off-targets hDHFR and hTS, by the folate-related anti-cancer agent methotrexate (MTX) and 7 pteridine-based reference compounds (**1**, **2**, **III**-**VII**, Figure **2AB** and Table **S1**, SI).[26,30,32] Although the seven reference compounds were primarily

designed as *Lm*PTR1 inhibitors, we found all except **VII** to be more potent against *Tb*PTR1 than *Lm*PTR1. **1** was the strongest inhibitor of *Tb*PTR1 with an IC_{50} of 50 nM against *Tb*PTR1 and 1 µM against *Lm*PTR1 (Figure **2A**).

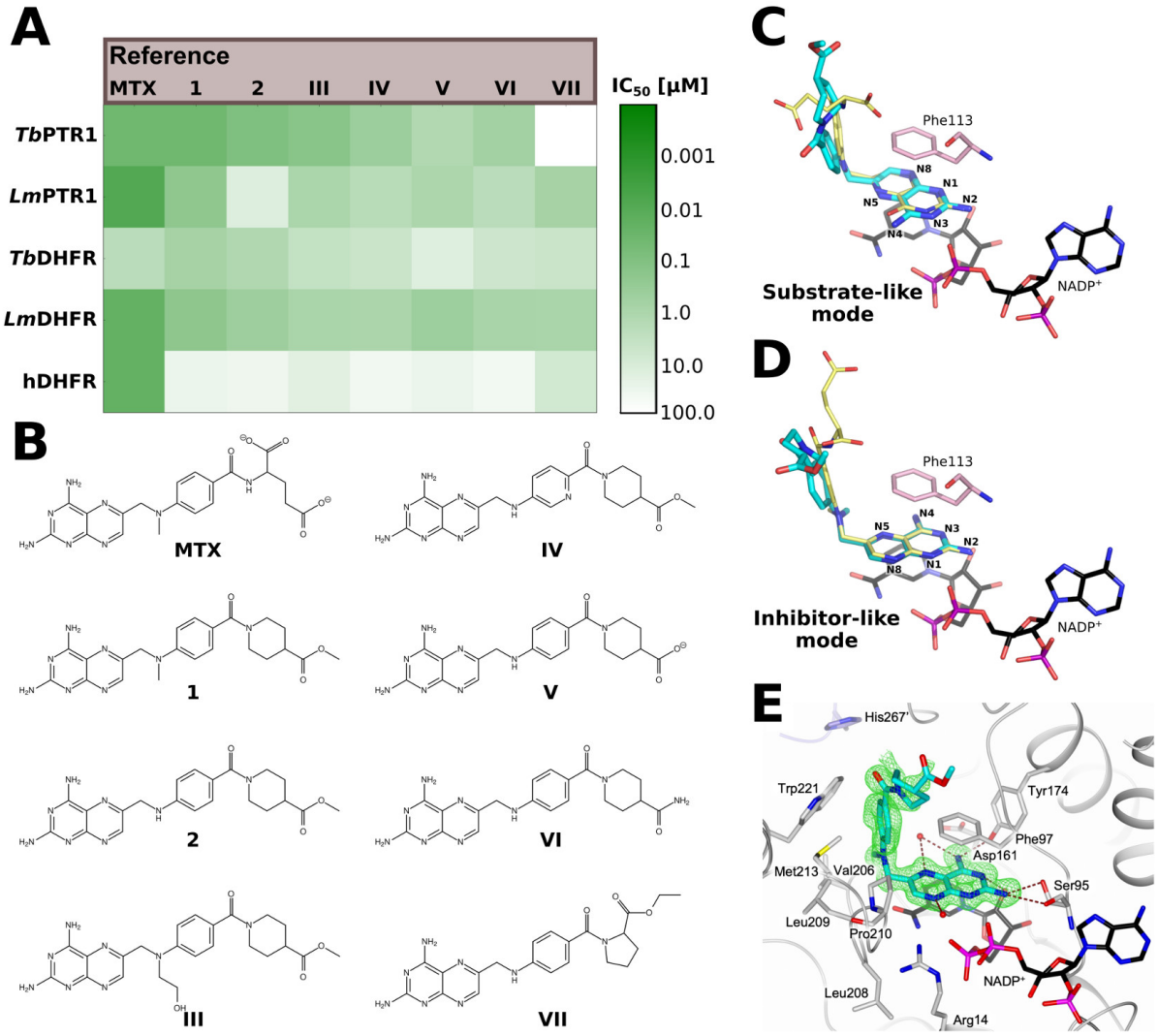

Figure 2. Inhibitory activities, structures and orientations of reference pteridines in crystal structures of *Lm*PTR1 (PDB-ID 2qhx) and *Tb*PTR1 (PDB-ID 6rx5). (A) The activity heatmap shows IC_{50} values in different targets and off-targets in µM, colored from green to white for low to high IC_{50}s. Values are reported for *Tb*PTR1, *Lm*PTR1, *Tb*DHFR, *Lm*DHFR and the off-target hDHFR. All values, as well as data for hTS, are reported in Table **S1**, SI. (B) The previously published compounds shown were used as references: **1**, **2** and **VII** are **6b**, **6a** and **6c** from Cavazzuti et al.[26] and **III**, **IV**, **V** and **VI** correspond to **5d**, **5b**, **6a** and **5a** from Corona et al.[30] (C) Compound **1** (cyan carbons) in its substrate-like conformation in *Lm*PTR1 with folate superimposed from *Tb*PTR1 PDB-ID 3bmc (yellow sticks); (D) Compound **1** (cyan carbons) in an inhibitor- or MTX-like orientation in *Lm*PTR1 with MTX superimposed from *Lm*PTR1 PDB-ID 1e7w (yellow sticks). The pteridine nitrogens are labeled according to the ring nomenclature. (E) Crystallographic complex of *Tb*PTR1 (gray cartoon, His267' from the neighboring subunit in lavender) in complex with NADPH/$NADP^+$ and compound **1** determined in this work. In *Tb*PTR1, compound **1** shows the MTX-like binding mode. Interacting residues (in C, D: only Phe113) and the NADPH/$NADP^+$ cofactor are shown in sticks (carbons colored according to protein and black, respectively). In (E), water molecules are shown as red spheres and the inhibitor is surrounded by the omit map (green wire) contoured at the 2.5 σ level. Hydrogen bonds are represented by brown dashed lines.

Notably, the reference compounds largely exhibited micromolar to submicromolar inhibition of *Lm*DHFR and *Tb*DHFR (IC_{50} *Lm*DHFR 0.3 – 1.4 µM; *Tb*DHFR 0.3 – 20.5 µM). While MTX was more potent against the parasite DHFRs, it was not selective (Selectivity index SI:

*Tb*DHFR/hDHFR 3 and *Lm*DHFR/hDHFR 1). Among the reference compounds, we observed selectivity indices of up to about 160-170 for *Tb*DHFR and *Lm*DHFR.

Previously determined crystal structures show that compounds **1** and **2** share a substrate-like pterin orientation in the complex with *Lm*PTR1.[26] Compound **1**, in addition, features a second, so-called inhibitor-like (or MTX-like) orientation, with the bicyclic ring system flipped by 180° and rotated by 30° (Figures **2CD** and **S1** of the SI).[26] Similar observations have been made in crystallographic complexes of *Tb*PTR1 with small pteridine-based inhibitors.[32] Our crystal structure of the ternary complex of *Tb*PTR1 with NADPH/$NADP^+$ and the reference compound **1** (PDB-ID 6rx5, resolution 1.42 Å, experimental details: Tables **S2**-**S3**, SI) confirms that the diaminopteridinyl moiety of **1** adopts only the MTX-like orientation (Figure **2E**), resembling its MTX-like binding mode in *Lm*PTR1 (Figures **2D** and **S2**, SI). Docking studies consistently indicated that the reference compounds adopt MTX-like binding modes in the different targets and the off-target hDHFR (Table **S4**, Figure **S5**, SI). Since the reference compounds showed micromolar to submicromolar inhibition of parasitic PTR1 and DHFR, whilst being modestly selective for parasite over hDHFR, we next aimed to improve the target inhibition profiles in a multitarget-based design approach.

Four series of compounds designed to improve dual target selective inhibition

To optimize the compounds for *Tb*PTR1/*Tb*DHFR and *Lm*PTR1/*Lm*DHFR while minimizing inhibition of hDHFR, we employed our published optimization guidelines for MTX-like scaffolds derived from the extensive comparison of on- and off-targets in the parasitic folate pathway:[31] Based on the overlapping properties in the different protein targets and differences between targets and off-targets, modifications for improved target interactions and selectivity were defined for **1** (Figure **3A**). We designed three series of compounds, each with modifications in one of three parts of the pteridines: the N10 position, the *para*-amino benzoic acid (PABA) moiety and the tail portion (Figure **3B**).

In the N10 series, five novel pteridines (**3**-**5**, **9** and **22**, Figure **3B**) were modified in the N10 position to improve interactions with PTR1 and parasite DHFR and to exploit the differing pocket sizes and residues in parasitic targets and the hDHFR off-target.[31] Nonpolar substitutions, like the ethyl and propargyl substituents of **3** and **5** were designed to interact with aliphatic residues surrounding N10 in the parasite targets, e.g. Leu209 of *Tb*PTR1; Ile47 and Leu90 of *Tb*DHFR; Leu226 and Leu229 of *Lm*PTR1; Ile20 and Val62 of *Lm*DHFR (Figure **3A**).

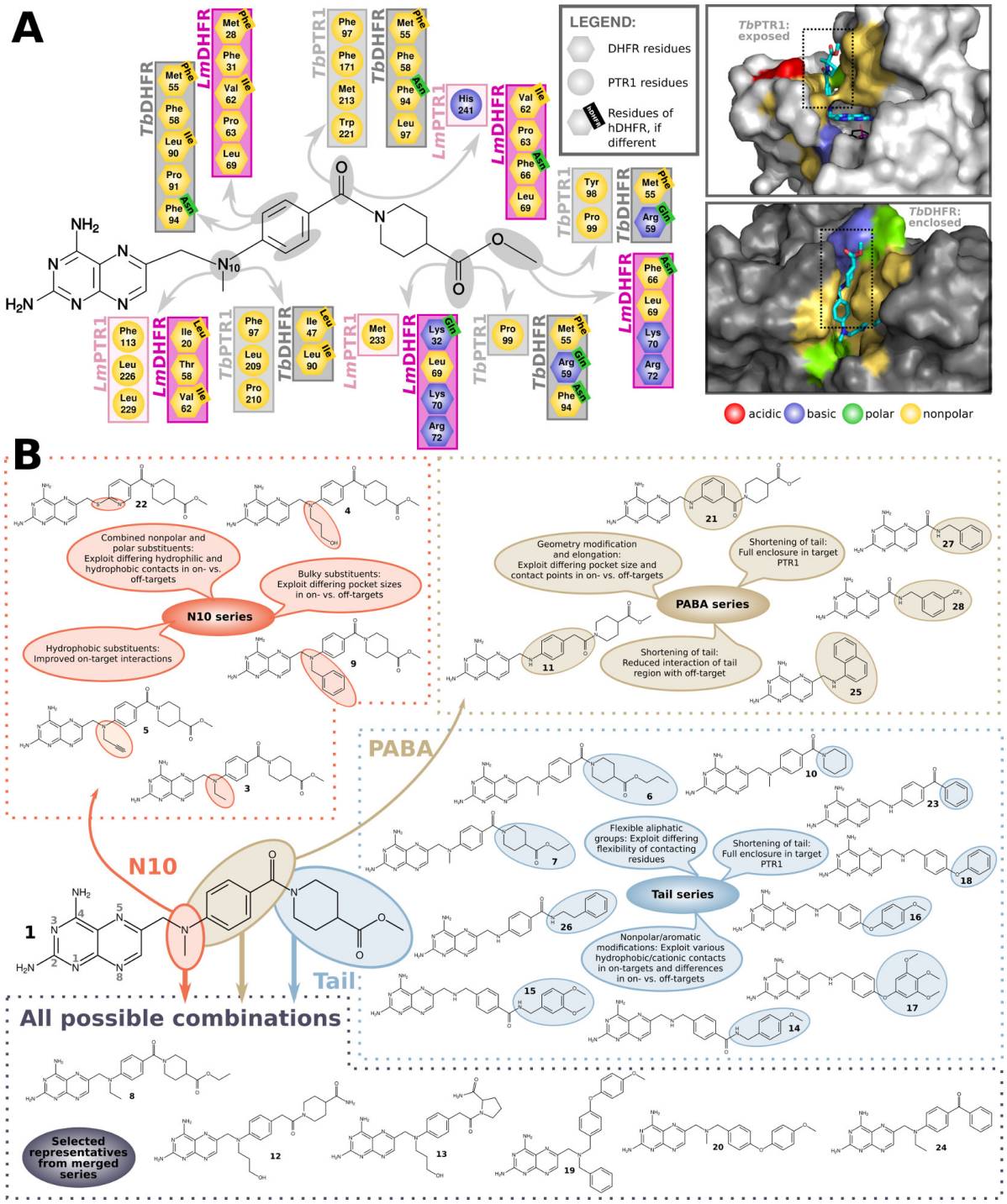

Figure 3. Structural features of PTR1 and DHFR considered in the multitarget design of selective compounds and overview of the modifications explored in four designed compound series, exemplified by highlighting on reference compound **1**. (A) Selected residues within 5 Å of the marked modification sites based on the bound orientations of **1** in *Tb*PTR1 (pale gray), *Tb*DHFR (dark gray), *Lm*PTR1 (light pink) and *Lm*DHFR (magenta). Based on Panecka-Hofman et al.[31], this map provides an overview of residues having similar properties in the surrounding of specific ligand portions in all targets (covering only those applied for the design as shown in (B), for full maps, see Figures **S3**,**S4**). In some positions, parasite DHFR differs in amino acid type from the off-target hDHFR, thus highlighting suitable substitution points to improve selectivity. Differing hDHFR residues are labeled in the top right corner of the corresponding parasite DHFR residue. A surface representation of complexes of **1** with *Tb*PTR1 (top right, PDB-ID 6rx5) and *Tb*DHFR (bottom right, MTX-like docking result that was top-ranked by the Glide docking score in PDB-ID 3rg9) highlights the solvent-exposure of the tail in PTR1, which is in contrast well-enclosed in DHFR. All residues in (A) are colored by type: red=acidic, blue=basic, green=polar, yellow=nonpolar. Compound **1** and the NADPH/NADP$^+$ cofactor are shown in sticks with cyan and black carbons, respectively. (B) Synthesized members of each designed series with the series for the three modification sites (N10, PABA, tail) shown in a framed box along with the key objectives addressed with the respective modifications. A fourth, merged series, shown at the bottom of the figure, was constructed by combining all modifications studied *in silico* in all possible permutations. Of the resulting 2014 compounds, six selected representatives were synthesized. The small gray numbers indicate the pteridine ring nomenclature.

The large benzyl substituent of **9** may in addition allow for enhanced selectivity due to the lower

volume of the hDHFR compared to the parasite DHFR pocket (pocket volume *Tb*DHFR 353 Å^3, *Lm*DHFR 384 Å^3 and hDHFR 347 Å^3). In **22**, we replaced N10 by sulfur and the PABA benzene ring by pyridine, to improve off-target selectivity. Whereas hDHFR favors hydrogen bond donors in the proximity of N10 and the PABA ring system, the parasite DHFRs show regions favorable for interaction with hydrogen bond acceptors.[31] Corona et al.[30] demonstrated improved selectivity for PTR1 over hDHFR by hydrophilic N10 substitutions. Our data for reference compound **III**, with a hydroxyethyl substituent, did not confirm this conclusion (Figure **2A**) and our docking simulations indicated that interaction with a conserved structural water might require an unfavorable conformation of the substituent (Figure **S5A**, SI). To improve interactions between the substituent and water, we therefore elongated the aliphatic linkage to a hydroxypropyl in **4**.

In the PABA series with 5 new pteridine derivatives (**11**, **21**, **25**, **27**-**28**, Figure **3B**), we explored modifications of the PABA moiety and the amide linkage to the tail portion. To improve selectivity by exploiting the different pocket sizes and contact points of hDHFR and the parasite proteins, in **11**, we replaced the PABA phenyl group with benzyl and, in **21**, the entire PABA moiety by a meta-aminobenzoic acid (Figure **3**). The compound tails are solvent-exposed in PTR1, thus having poorly defined interactions (Figure **3A**), whereas strong interactions occur with the hDHFR off-target.[31] We therefore shortened the tail region to achieve full enclosure in the PTR1 binding pocket by replacing PABA by naphthalene or benzene (non-substituted or substituted with -CF_3; **25, 27** and **28**, respectively).

In the tail series, we explored tail modifications resulting in 10 additional new pteridines (**6**-**7**, **10**, **14**-**18**, **23** and **26**, Figure **3B**). In both *T. brucei* targets, hydrophobic contact points accessible to the compound tail region exist (Figure **3A**). Since the flexibility of the tail likely contributes entropically to binding affinity in PTR1, directional interactions of the tail may be unfavorable. Hydrophobic interactions are geometrically less restrained than, for instance, hydrogen bonds, and thus less likely to entropically penalize binding. Therefore, the methyl ester in the tail of **1** was replaced by the more flexible ethyl and propyl in **7** and **6**, respectively. Additionally, in parasite DHFR, the tail is enclosed by more hydrophobic moieties than in the hDHFR off-target (Figure **3A**) and the surrounding residues show different conformational variability in the crystal structures, which suggests further on/off-target selectivity benefits.[31] Combining the exploitation of these differences with improved enclosure in PTR1 (Figure **3A**), we modified the tail to an unsubstituted piperidine (**10**) or replaced piperidine with an unsubstituted benzene (**23**). Compound **26**, with benzene attached via a flexible ethyl linkage to an MTX-like amide, can benefit from nonpolar and aromatic contact points in PTR1 and DHFR and adapt to their differing placement. The flexible aromatic tail may further form cation-π interactions with positively charged residues in the entrance of the DHFR pocket (Figure **3A**). In compounds **14** and **15**, we explored an altered geometry with a one-carbon spacer

between N10 and PABA and amide-linked methoxylated tail portions (Figure **3B**). The methoxylations may form additional contacts with hydrophobic residues in the target pocket entrance regions (e.g. Pro99 of *Tb*PTR1, Figure **3A**). In addition, an etheryl linkage to a non-substituted (**18**), methoxylated (**16**) or trimethoxylated (**17**) benzyl group was explored to likewise exploit hydrophobic, aromatic and positively charged contact points found around the tail region in the various targets (Figure **3A**).

In a fourth series, the 'merged' series, the modifications in the above three series were permuted and merged by decomposing the compounds into fragments and recombining them *in silico* in all possible combinations of these fragments (see details in the SI). The 2014 compounds generated were filtered based on docking results and physico-chemical properties and, of the remaining 600 candidates, six were selected for synthesis: Two compounds (**12** and **13**, Figure **3B**) were chosen for their favorable interaction patterns and scores predicted by docking simulations, while four other compounds (**8**, **19**, **20** and **24**, Figure **3B**) were selected based on physicochemical marker properties that show some correlation with *in vitro* anti-parasitic activity as described below. **12** combined the N10 hydroxypropyl substituent of **4**, the tail carboxamide group of **VI** and the elongation by a carbon spacer in the PABA moiety of **11**. The same combination with a pyrrolidine replacing piperidine, like in reference compound **VII,** additionally gave **13**. Similarly, the ethyl modification of N10 in **3** and the ethyl ester in the tail fragment of **7** were joined to give **8**, which largely addressed the hydrophobic contact points in different targets. The ethyl modification of N10 was also joined with the shortened tail of **23** to give compound **24**. Finally, the N10 benzyl-substitution of **9** and the methyl of the reference compound **1** were joined with the PABA and tail-modified scaffold of **16** to give **19** and **20**, respectively.

Synthesis of pteridine derivatives with high yield

26 new 2,4-diaminopteridine derivatives and the reference compounds **1** and **2** were (re)synthesized as reported in Schemes **1**-**8**. Our methodology for improved reaction yield of the chemical pteroid step was applied to provide a key intermediate for most designed compounds.[33] Displacement of the chloride of the 6-(chloromethyl)pteridine-2,4-diamine hydrochloride (**29,** Scheme **1**) by the appropriate substituted anilines and aliphatic amino-derivatives was carried out in N,N-dimethylacetamide (DMA) at 60°C microwave (MW) to provide the desired target compounds **1**-**26** in high yields of 70−90% with reduced reaction time (Schemes **2**-**7**).[33]

The PABA amine functionalization was achieved by selective alkylation of primary amines to secondary amines using nitriles as an alkylating reagent with Pd/C for intermediates **32-33**.[34,35] Conventional alkylation of the latter with propargyl bromide or (bromomethyl)benzene resulted in derivatives **34** and **35**, respectively (Scheme **2**).

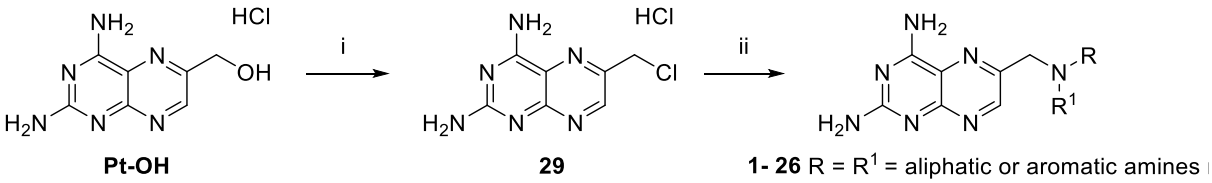

Scheme 1. Synthesis of derivatives of compound **29**. Reagents and conditions: (i) $SOCl_2$, reflux, 12 h. 70% yield; (ii) **29** (1.2 equiv.), K_2CO_3 (3 equiv.), KI (0.1 equiv.), DMA, 60°C, 20'-30' MW.

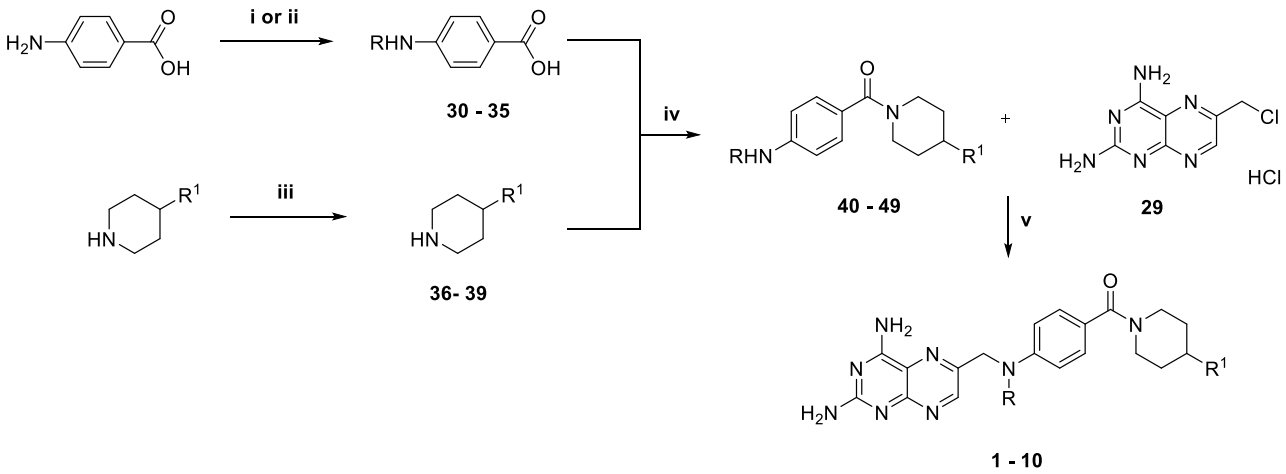

R=	CH_3	R^1=	$COOCH_3$	ID=	1	Reagents=	30	36	40
	H		$COOCH_3$		2		31	36	41
	CH_2CH_3		$COOCH_3$		3		32	36	42
	$CH_2CH_2CH_2OH$		$COOCH_3$		4		33	36	43
	CH_2CCH		$COOCH_3$		5		34	36	44
	CH_3		$COOCH_2CH_2CH_3$		6		30	37	45
	CH_3		$COOCH_2CH_3$		7		30	38	46
	CH_2CH_3		$COOCH_2CH_3$		8		32	38	47
	$CH_2C_6H_5$		$COOCH_3$		9		35	36	48
	CH_3		H		10		30	39	49

Scheme 2. Synthesis of compounds **1**-**10**. Reagents and conditions: **30**, **31**, **36** and **39** were purchased from Sigma; (i) acetonitrile or 3-hydroxypropanenitrile, 10% Pd/C, NH_4OAc (1 equiv.), CH_3OH, H_2, rt, 24-36 h (**32**-**33**); (ii) alkyl halide (propargyl bromide, (bromomethyl)benzene) (0.5 equiv.), K_2CO_3 (2 equiv.), DMF dry, rt, 24 h (**34**-**35**); (iii) $SOCl_2$ (4 equiv.), propanol (for **37**), EtOH (for **38**), reflux, 7-12 h; (iv) EDC·HCl (1.1 equiv.), HOBt (0.1 equiv.), TEA (2-3 equiv.), DMF, rt, overnight (**40**-**49**); (v) **29** (1.2 equiv.), K_2CO_3 (3 equiv.), KI (0.1 equiv.), DMA, 60°C, 20' MW (**1**-**10**).

The reductive alkylation of amines using nitriles was also used to obtain **51** and **74** in Schemes **3** and **7**. The isonipecotic acid derivatization was achieved via Fischer esterification using the reagent-solvents propanol (**37**) and EtOH (**38**), respectively; methyl isonipecotate (**36**) and piperidine (**39**) were purchased from Sigma (Scheme **2**). The intermediate acid derivatives **30-35, d-e** were condensed to amides through a coupling reaction with the respective amines **36-39** and **g** using EDC·HCl in dimethylformamide (DMF) as the coupling agent to provide the intermediate products **40**-**49**, **71-72** and **75**, which were then made to react with **29** to obtain the final compounds (**1-10, 21-22, 26**; Schemes **2**, **6**, **7**).

Using the same method, we synthesized the elongated compounds **11-15** characterized by a carbon spacer in the PABA moiety (Scheme **3-4**). To obtain compounds **14-15** (Scheme **4**), an additional protection step reaction to guide selective amide functionalization was necessary. The selectivity was thereby achieved by a Boc-protection in the first step of the reaction of **b** to obtain **55**, which was then coupled with the respective aliphatic amine to give compounds **56-57**. The target amines were finally obtained by a deprotection step carried out in 30−40% trifluoroacetic acid/dichloromethane (TFA/DCM) in quantitative yield.

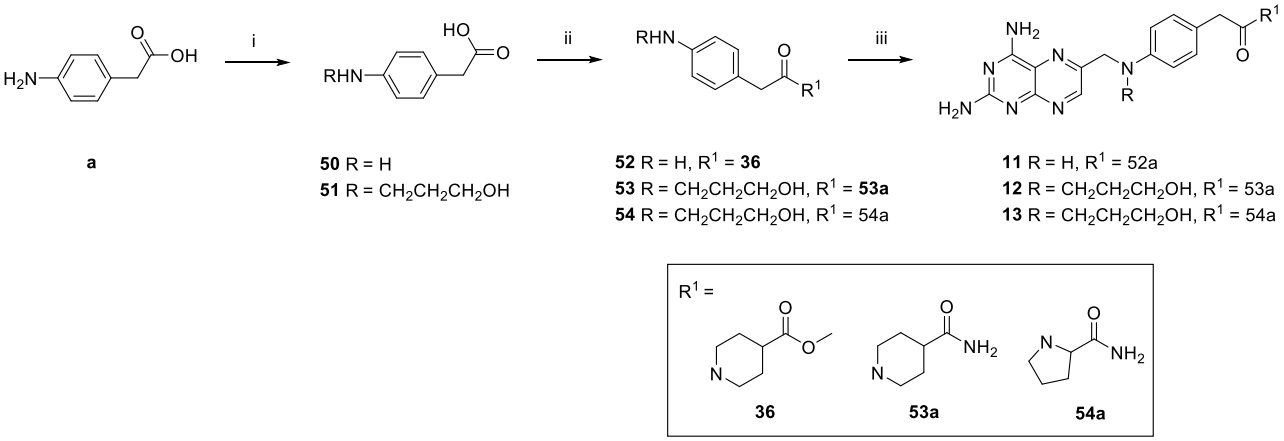

Scheme 3. Synthesis of analogs **11-13**. Reagents and conditions: (i) 3-hydroxypropanenitrile, 10% Pd/C, NH_4OAc (1 equiv.), CH_3OH, H_2, rt, 24 h (**51**); (ii) EDC·HCl (1.1 equiv.), HOBt (0.1 equiv.), TEA (2-3 equiv.), DMF, rt, overnight (**52-54**); (iii) **29** (1.2 equiv.), K_2CO_3 (3 equiv.), KI (0.1 equiv.), DMA, 60°C, 20' MW (**11-13**).

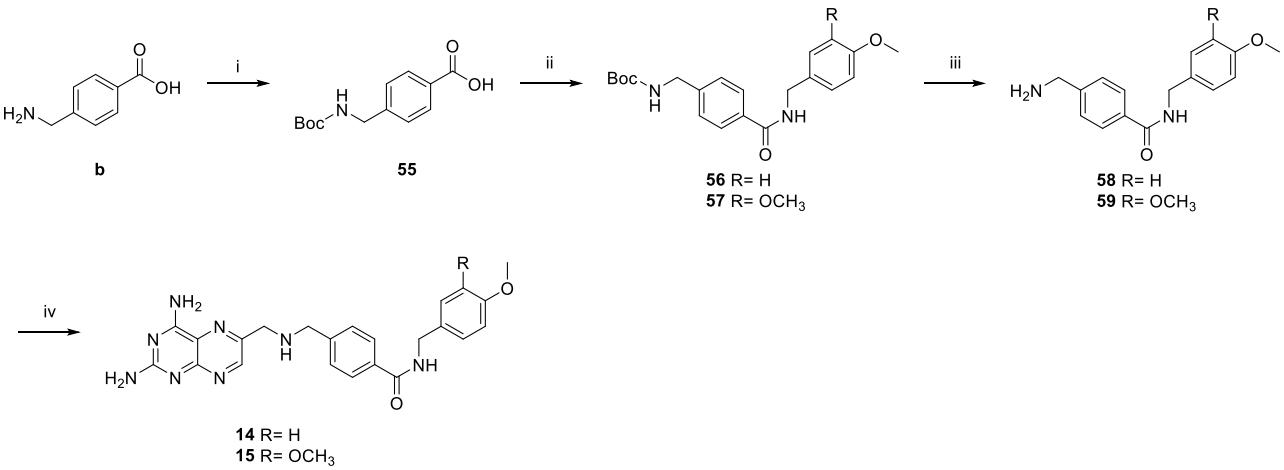

Scheme 4. Synthesis of analogs **14-15**. Reagents and conditions: (i) di-tert-butyl pyrocarbonate (1.05 equiv.), dioxane\H_20\1N NaOH 1\1\1 V\V\V, rt, 6h (**55**) (i) EDC·HCl (1.1 equiv.), HOBt (0.1 equiv.), TEA (2-3 equiv.), DMF, rt, overnight (**56-57**); (iii) TFA, DCM, rt; (**58-59**); (iv) **29** (1.2 equiv.), K_2CO_3 (3 equiv.), KI (0.1 equiv.), DMA, 60°C, 20' MW (**14-15**).

The phenoxyphenyl-methanamine derivative intermediates (Scheme **5**) were synthesized starting from 4-fluorobenzaldehyde and the respective phenol derivates **60-62** by an S_NAr reaction. Subsequently, the primary amines **66-68**[36], or functionalized amines **69-70** via a one-pot reductive step, were reacted with **29** to obtain compounds **16-20**. Compounds **23-25**, with a higher steric hindrance, were obtained with slightly

increased reaction time in a good yield. Finally, to obtain compounds **27-28**, it was required to first perform an oxidation reaction. Treatment of Pt-OH in acetone/0.5 M phosphate buffer at pH 7 (1:1 v\v) with $KMnO_4$ gave the oxidized analog **76**, which was subsequently coupled with the selected aliphatic amine to obtain the desired amides (Scheme **8**).

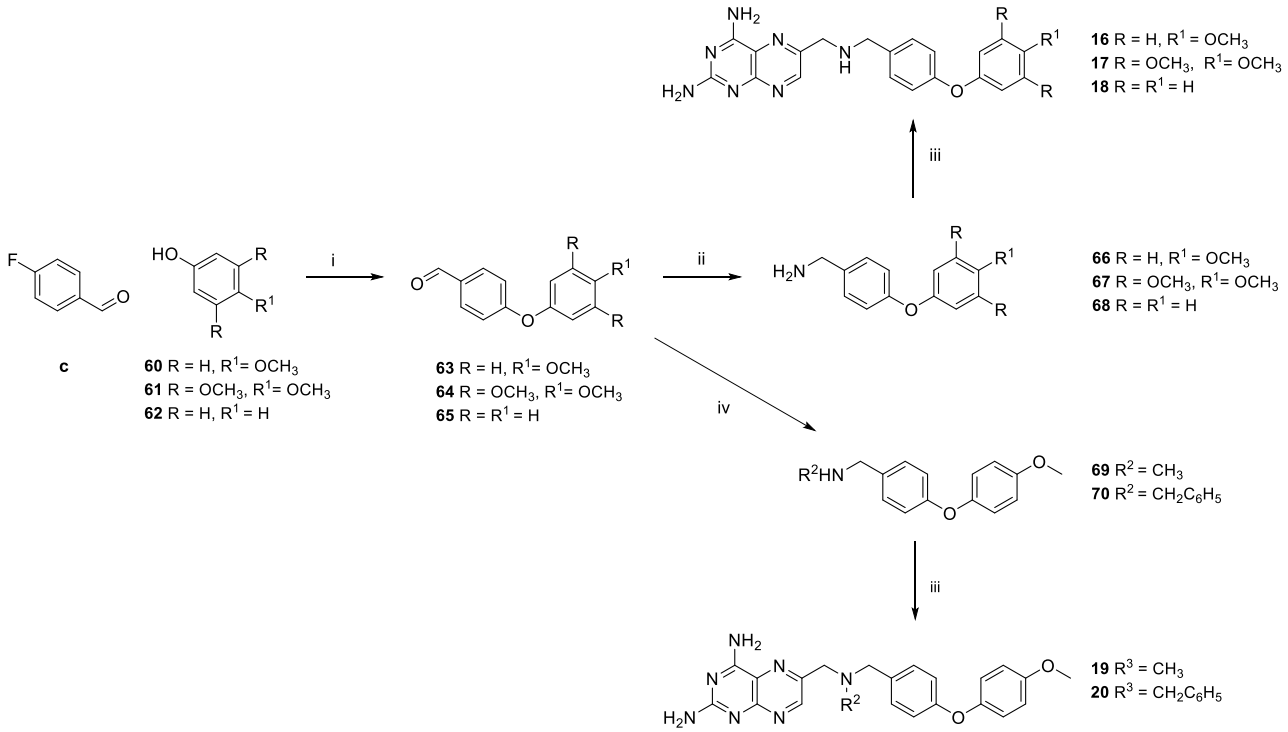

Scheme 5. Synthesis of analogs **16**-**20**. Reagents and conditions: (i) K_2CO_3 (3 equiv.), DMF, reflux, 16-18 h (**63**-**65**); (ii) $NH_2OH.HCl$ (1.2 equiv.), EtOH, rt, > 1 h followed by Zn dust (2.5 equiv.) in 12 M HCl (4 equiv.), rt, 15' (**66**-**68**); (iii) **29** (1.2 equiv.), K_2CO_3 (3 equiv.), KI (0.1 equiv.), DMA, 60°C, 20' MW (**16**-**20**); (iv) methylamine (for **69**) or benzylamine (for **70**) EtOH dry, 60°C, 3 h, then $NaBH_4$ (1.5 equiv.), rt, 2h.

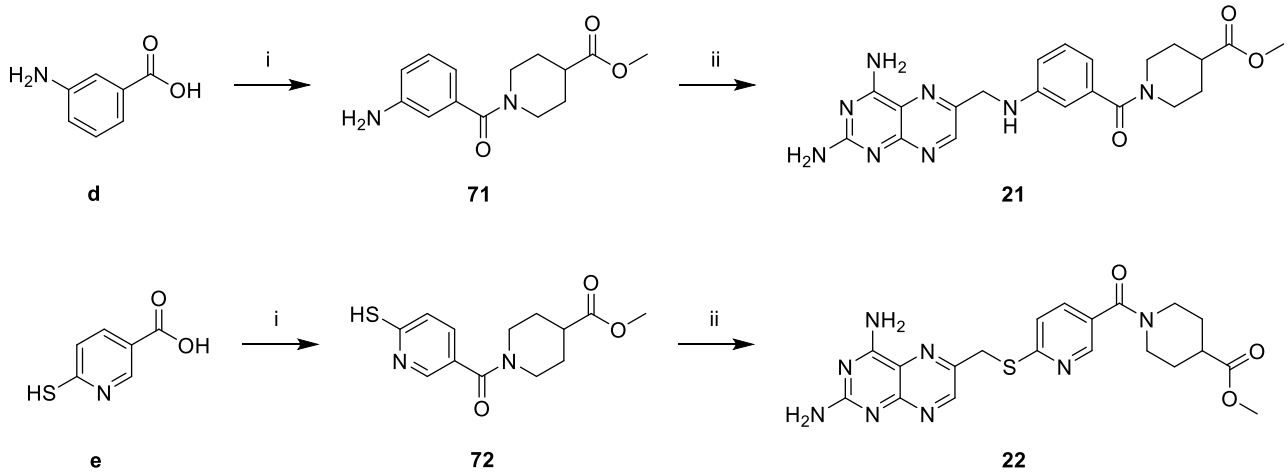

Scheme 6. Synthesis of analogs **21**-**22**. Reagents and conditions: (i) EDC·HCl (1.1 equiv.), HOBt (0.1 equiv.), TEA (2-3 equiv.), DMF, rt, overnight (**71**-**72**); (ii) **29** (1.2 equiv.), K_2CO_3 (3 equiv.), KI (0.1 equiv.), DMA, 60°C, 20' MW (**21**-**22**).

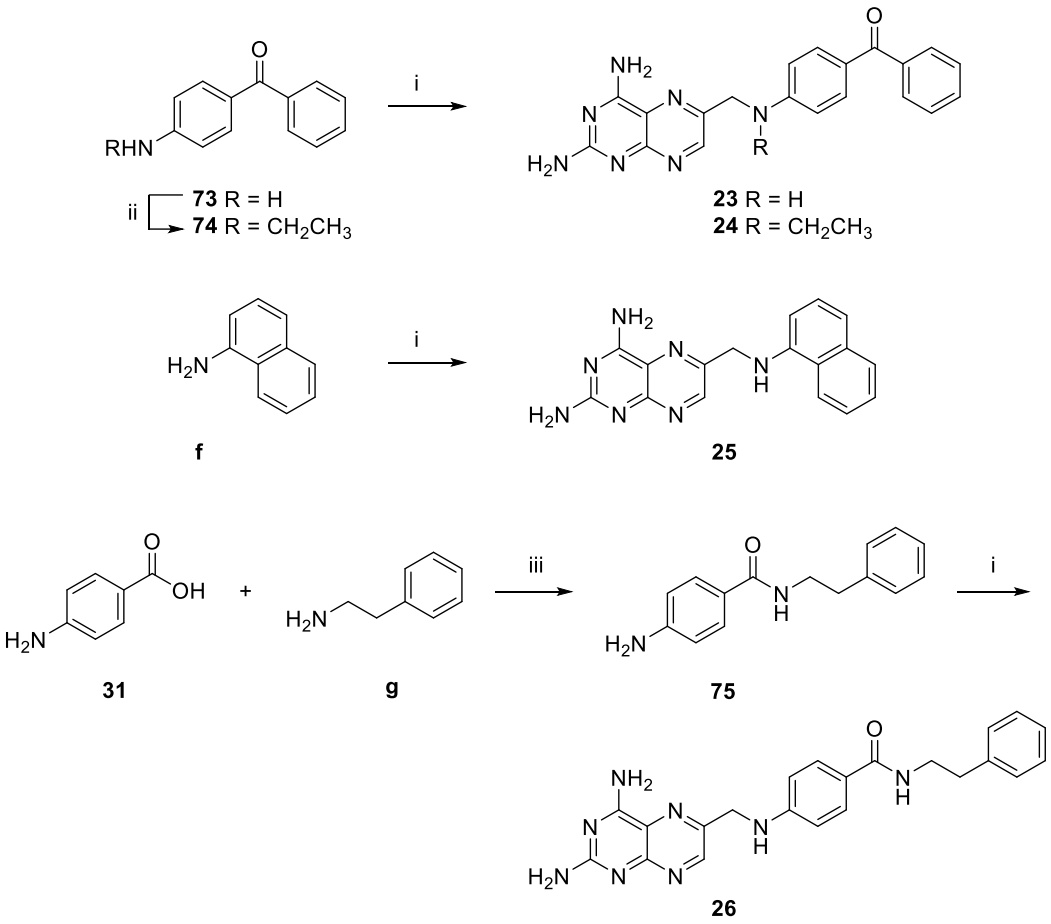

Scheme 7. Synthesis of analogs **23**-**26**. Reagents and conditions: (i) **29** (1.2 equiv.), K_2CO_3 (3 equiv.), KI (0.1 equiv.), DMA, 60°C, 20'-30' MW (**23**-**26**); (ii) acetonitrile, 10% Pd/C, NH_4OAc, CH_3OH, H_2, rt, 24-36 h (**74**); (iii) EDC·HCl (1.1 equiv.), HOBt (0.1 equiv.), TEA (2-3 equiv.), DMF, rt, overnight (**75**).

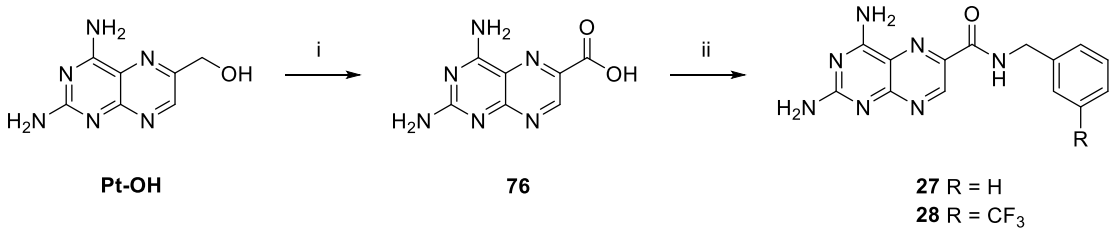

Scheme 8. Synthesis of analogs **27**-**28**. Reagents and conditions: (i) $KMnO_4$, acetone/0.5 M phosphate buffer at pH 7 (1:1 V\V); (ii) EDC·HCl (1.1 equiv.), HOBt (0.1 equiv.), TEA (2-3 equiv.) DMF, rt, overnight.

Designed pteridine derivatives have improved on-target and off-target enzyme inhibitory activity profiles and bind in an MTX-like orientation

The measured inhibitory activities of compounds **3**-**28** against the targets *Tb*PTR1, *Tb*DHFR, *Lm*PTR1, *Lm*DHFR, and the off-targets hDHFR and hTS, are given in Figure **4** and Table **S1**. Most of the new pteridine derivatives displayed 1–2-fold greater inhibition of *Tb*PTR1 than *Lm*PTR1 and were more or equally active against PTR1 than the reference compound **1**. The inhibitors with nanomolar to picomolar PTR1 inhibition showed improved selectivity for PTR1 over the off-target hDHFR by up to about 3 orders of magnitude. The activities against *Tb*DHFR

and *Lm*DHFR exceeded those against hDHFR, where the IC_{50} was typically worse than 100 µM. For parasite DHFR, the best compounds were overall similar to **1**: compound **8** with an IC_{50} of 0.23 µM against *Tb*DHFR and **6**, **7**, **8** and **24** with IC_{50}s of 0.13-0.23 µM against *Lm*DHFR (compared to **1**: 0.3 µM for both *Tb*DHFR and *Lm*DHFR). Only compound **13** was slightly more selective for *Tb*DHFR than **1** with an SI of 169 (compared to 164). Docking studies suggested that the majority of the novel pteridines adopted MTX-like binding modes in both PTR1 and parasite DHFR variants and the off-target hDHFR (see docking results, Tables **S5**, **S6**, SI).

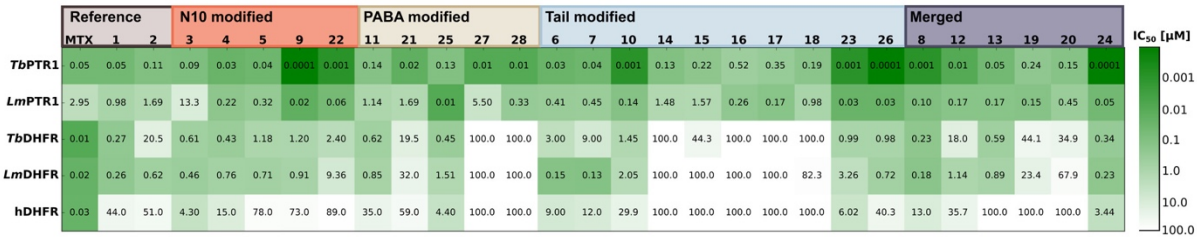

Figure 4. Inhibitory activities of compounds of the designed N10-, PABA-, and tail-modified series, the merged series, and selected reference compounds. The activity heatmap shows IC_{50} values in different targets and off-targets in µM, colored from green to white for low to high IC_{50}s. Values are reported for *Tb*PTR1, *Lm*PTR1, *Tb*DHFR, *Lm*DHFR and the off-target hDHFR. All values, as well as data for hTS, are reported in Table **S1**.

Pteridine derivatives 3 and 4 bind in an MTX-like orientation in both PTR1 variants. The structures of *Tb*PTR1 with the new pteridines **3** and **4**, and that of *Lm*PTR1 with **4**, were determined to 1.20 Å, 1.11 Å and 2.10 Å resolution, respectively (see Tables **S2**-**S3**). The overall structure of the *Tb*PTR1 complexes resembles the complex with **1** (compare Figure **2E** with **5A**). The N-ethyl moiety of **3** forms van der Waals interactions with Val206 and Trp221 on the hydrophobic side of the pocket (Figure **5A**). The bulkier N-propylhydroxyl moiety of **4** forms direct and water-mediated hydrogen bonds with Asp161 and receives an intramolecular hydrogen bond from the amine in position 4 on the pteridine system.

The structural characterization of *Lm*PTR1 in complex with **4** (Figure **5B**) shows the presence of a functional enzyme tetramer in the crystal asymmetric unit with a similar structure to those previously determined.[37,38] The MTX-like binding mode adopted by **4** in *Lm*PTR1 closely resembles that observed in *Tb*PTR1 except for the terminal piperidine moiety (Figure **S2CD** of the SI). The latter is highly flexible and was only poorly visible in our models - a possible orientation is reported, but further orientations cannot be excluded.

N10 modifications yield improved PTR1 inhibitors with similar trends for DHFR selectivity. The N10-modified compounds (**3**-**5**, **9** and **22**; Figure **3B**) were improved PTR1 inhibitors in comparison to **1** with the exception of **3** (**1** IC_{50} *Tb*PTR1 50 nM, *Lm*PTR1 1 µM; N10 series IC_{50} *Tb*PTR1 <0.1 - 90 nM; *Lm*PTR1 0.02-13.3 µM). **9** was the best in the series with a picomolar IC_{50} against *Tb*PTR1 and an IC_{50} of 20 nM against *Lm*PTR1.

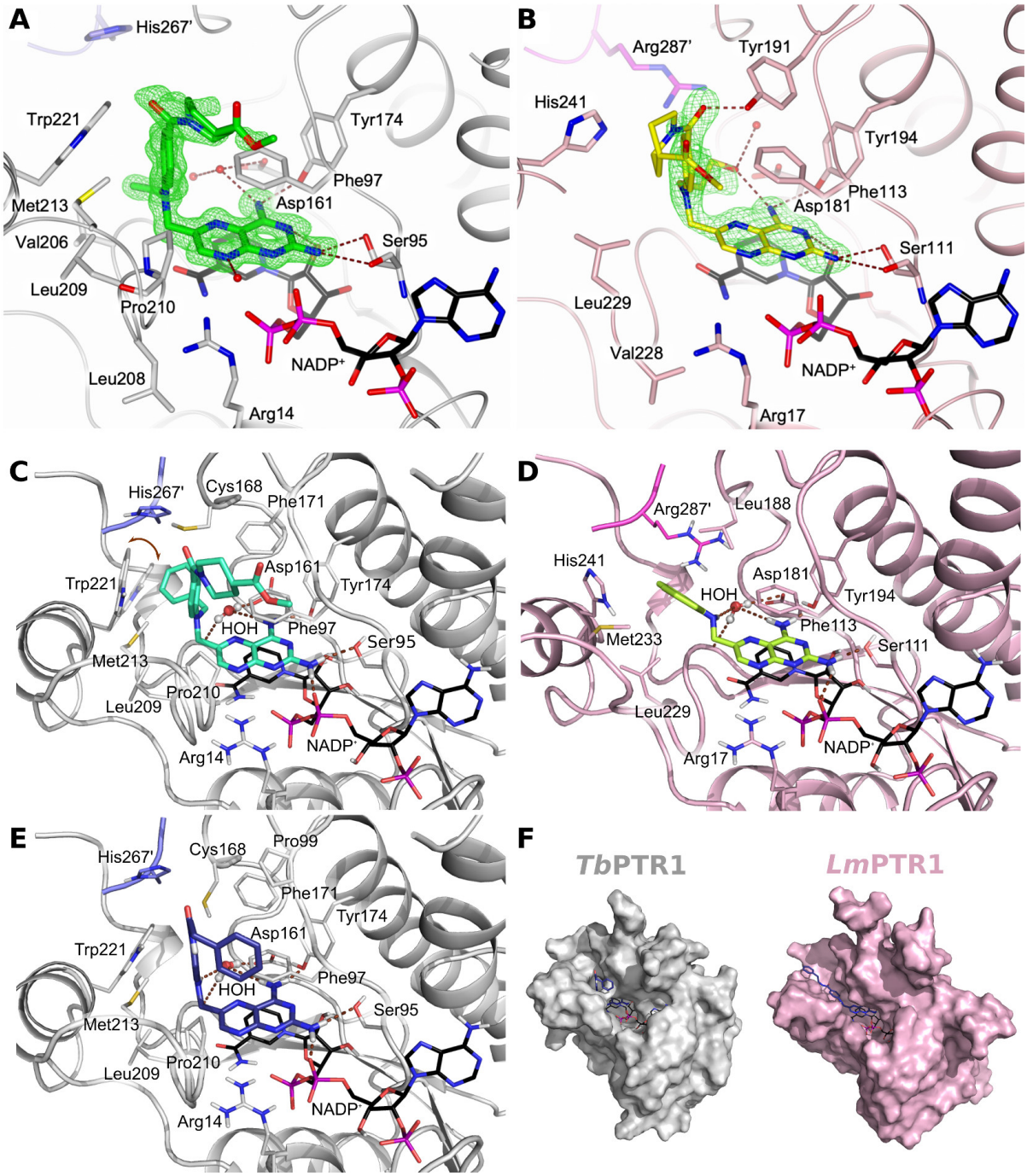

Figure 5. Orientations of pteridine-based inhibitors in *Tb*PTR1 and *Lm*PTR1 based on crystallographic complexes (A, B) and docking solutions (C-E) and comparison of pocket shape for the PTR1 variants (F). (A, B) Crystallographic complexes determined in this work show the MTX-like binding modes for both *Tb*PTR1 (A, gray cartoon, His267' from the neighboring subunit in lavender) and *Lm*PTR1 (B, pink cartoon, Arg287' from the neighboring subunit in magenta) in complex with NADPH/$NADP^+$ and the inhibitors **3** (A, green) and **4** (B, yellow). Water molecules are shown as red spheres and the inhibitors are surrounded by the omit map (green wire) contoured at the 2.5 σ level. (C) Induced fit (IF) MTX-like docking solution for compound **9** in *Tb*PTR1 in the presence of a conserved water molecule (ball-and-stick representation): Trp221 moves (indicated by a brown arrow) to make room for the phenyl of **9**. (D, E) Docking poses of: **25** (D, lime carbons) in *Lm*PTR1 and **26** (E, dark purple carbons) in *Tb*PTR1. All presented docking solutions were obtained in the presence of conserved structural water. Similar poses were generally observed in the docking without water. (F) Differing shape of the binding pocket in the two PTR1 variants: The compounds (in the example, **26**) show conserved core interactions in both PTR1s and their tails orient along the elongated binding site funnel in *Lm*PTR1, whereas the tail conformations in *Tb*PTR1 are typically kinked. Proteins are shown in surface representation. In all panels, interacting residues and the NADPH/$NADP^+$ cofactor are shown in sticks (carbons colored according to protein and black, respectively). Hydrogen bonds are represented by brown dashed lines. Docking results are only presented for N1-deprotonated compounds, but similar orientations were observed for the N1-protonated variants (see Figure **S6**). Further IF docking solutions are shown in Figures **S7**, **S8**.

The predicted orientations of the compounds in PTR1 were overall similar to the crystallographic data (Figure **5AB**), commonly showing the MTX-like orientation. **9**, when docked in presence of conserved structural water, was an exception due to its bulky benzyl substituent and required the reorganization of Trp221 in *Tb*PTR1 (see the induced fit docking pose in Figure **5C**). This reorganization is plausible since Trp221 was previously identified as a flexible residue in the *Tb*PTR1 pocket gating region on the basis of crystallographic data.[32]
All compounds were roughly similar to **1** in parasite DHFR inhibition (**1** IC_{50} *Tb*DHFR and *Lm*DHFR 0.3 µM; N10 series IC_{50} *Tb*DHFR 0.4-2.4 µM, *Lm*DHFR 0.5-9.4 µM). The trends observed for parasite DHFR were however reflected in similar changes of the hDHFR inhibition and selectivity ranged from 7- to 66-fold for *Tb*DHFR and 9- to 110-fold for *Lm*DHFR over hDHFR, which was lower than for **1** (SI *Tb*DHFR/hDHFR 164 and *Lm*DHFR/hDHFR 167). Thus, mainly PTR1 inhibition benefited from the selected N10 modifications.

PABA modifications lead to strong variations in the target inhibition profile. The modifications of the PABA moiety in the PABA series (compounds **11**, **21**, **25**, **27** and **28**; Figure **3B**) distinctly affected the target activities. Particularly smaller, well-enclosed compounds showed varying activity improvement for different PTR1s: **25**, in contrast to most of the studied pteridines, was 13-fold more potent towards *Lm*PTR1 than *Tb*PTR1 (IC_{50} 10 nM and 130 nM, respectively) and benefits from its steric fit to the elongated *Lm*PTR1 binding pocket (Figure **5DF**). The small, fully enclosed **27** and **28** were stabilized by hydrophobic residues lining the pocket entrance of *Tb*PTR1 (see Figure **3A**), which results in an around 10-fold higher potency than for reference compound **2** with the corresponding N10 substitution (IC_{50} **27**, **28**: 10 nM; **2**: 110 nM).
Against *Lm*DHFR, **25** showed similar activity to **2** (IC_{50} 1.5 and 0.6 µM, respectively), whereas it displayed higher activities for both *Tb*DHFR (IC_{50} **2**: 20.5 µM; **25**: 0.5 µM) and hDHFR (IC_{50} **2**: 51 µM; **25**: 4 µM). A one-carbon spacer to shift the position of the PABA carbonyl in **11** retained the *Lm*DHFR activity similar to **2** (**11**: IC_{50} 0.8 µM) but increased the inhibition of *Tb*DHFR (IC_{50} 0.6 µM). While the compounds were generally well stabilized by hydrophobic interactions in all DHFR variants, differences in pocket size and surrounding residue patterns in the proximity of the PABA moiety (Figure **3A**) modulate the differing activity profiles.

Alterations in tail geometry boost PTR1 inhibition but can reduce DHFR activity. In the tail-modified series (compounds **6**-**7**, **10**, **14**-**18**, **23** and **26**; Figure **3B**), hydrophobic and aromatic residues lining the pocket entrance region of PTR1, like Tyr98, Pro99 and Phe171 of *Tb*PTR1 or Met233 and His241 of *Lm*PTR1 (Figure **3A**) were exploited by either tail elongation or shortening. Interactions of these residues with the flexible aromatic tail of **26** (Figure **5EF**) likely contribute to the boost of the IC_{50} against *Tb*PTR1 to the picomolar range and to 30 nM

against *Lm*PTR1 – a more than 1000-fold and 57-fold improvement, respectively, in PTR1-inhibitory potencies compared to reference compound **2**. The shortened tails of **10** (unsubstituted piperidine) and **23** (benzene) were stabilized by the same residues and benefit from a better enclosure in the PTR1 pocket. Both compounds show increased *Tb*PTR1 and *Lm*PTR1 inhibition when compared to **1** (IC_{50} *Tb*PTR1 **10**, **23**: 1 nM both vs. **1**: 50 nM; *Lm*PTR1 **10**: 0.1 µM, **23**: 0.03 µM vs. **1**: 1.0 µM).

Tail shortening diminished the inhibition of parasite DHFR, whereas it did not affect or even increased the effect on the off-target hDHFR. The piperidine/benzene groups in the tails of **10** and **23** can form more extended hydrophobic interactions with Phe31 of hDHFR than with the corresponding methionine in the parasite DHFR variants (Figure **6**). In the parasite protein, moreover, Asn64 in the pocket entrance of hDHFR is replaced by phenylalanine, which, upon interaction with the compound tail, becomes solvent-exposed. The aforementioned pocket size and interaction pattern differences between *Lm*DHFR and other DHFR variants (Figure **3A**) also affected the tail series: For instance, **23** was more active against both *Tb*DHFR and hDHFR than **2** (IC_{50} *Tb*DHFR 1 vs. 21 µM, hDHFR 6 vs. 51 µM), while both compounds showed similar activity for *Lm*DHFR.

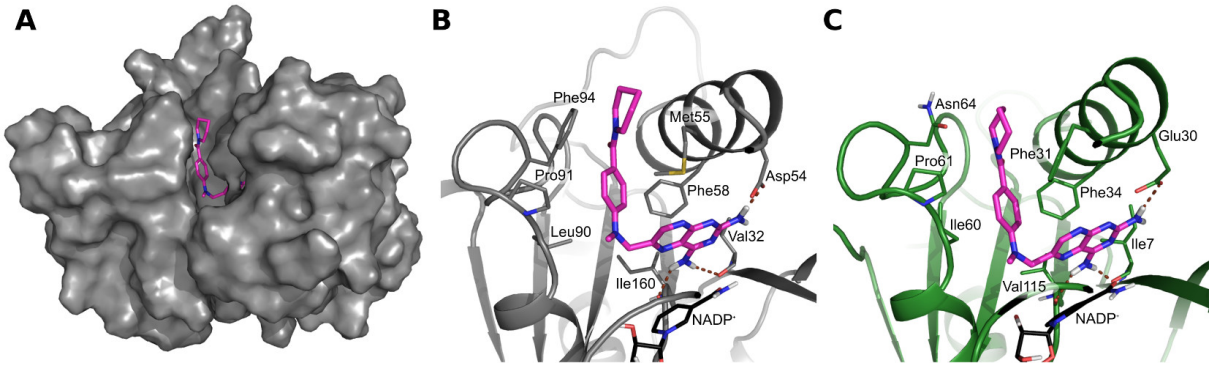

Figure 6. Docking results for compound **10** from the tail series (magenta sticks) in *Tb*DHFR (A, B) and hDHFR (C). (A) The *Tb*DHFR pocket accommodates **10** with its tail enclosed by surrounding residues. hDHFR has a similar shape. *Tb*DHFR is shown in gray surface representation. (B, C) *Tb*DHFR and hDHFR are shown in cartoon representation in gray and green, respectively. Important interacting residues and the NADPH/$NADP^+$ cofactor (black carbons) are shown as sticks. Hydrogen bonds are indicated by brown dotted lines. While the orientation of **10** is rather similar in both DHFR variants, the compound tail is more solvent-exposed in *Tb*DHFR: The PABA benzene and piperidine of **10** compete for interactions with Phe94 of *Tb*DHFR, which thereby becomes exposed to the solvent. In hDHFR, the corresponding exposed residue is the polar Asn64 and the tail of **10** can interact with Phe31 deeper in the pocket, rendering the mode of binding more favorable in hDHFR. The results are presented for N1-deprotonated compounds, but similar observations were made with N1 protonation (Figure **S6**).

Specific combinations of modifications lead to improved on-target inhibition and selectivity. Since the crystal structures and docking studies suggested a preference of the MTX-like orientation in all receptors, we used constrained docking to evaluate this binding mode for all 2014 members of the *in silico* library, containing all possible combinations of merged compound fragments explored in the N10, PABA and tail series. In most cases, MTX-like orientations with good scores were obtained and, therefore, the docking alone did not allow us to rule out many of the compounds. However, by combining a docking criterion with property and liability filters, we obtained 600 promising candidates composed of fragments of existing compounds in new combinations (Figure **7A**). Of these, six compounds with a diverse set of properties were selected for synthesis and further studies based on expert opinion.

Compounds **12** and **13** (Figure **3B**) combined fragments of **4**, **11**, reference **VI**, and, for **13**, in addition, reference **VII**. The activities and predicted interactions in all parasite targets were most reminiscent of **4**, suggesting the key importance of the hydroxy-propyl substituent to N10 for the target inhibition. Notably, while **12** was poorly selective for *Tb*DHFR (2-fold) and modestly selective for *Lm*DHFR (31-fold), **13** was inactive against hDHFR, resulting in a SI of 170 and 113 for *Tb*DHFR and *Lm*DHFR, respectively. Moreover, the compound had SIs over hDHFR of about 2000 for *Tb*PTR1 and 588 for *Lm*PTR1. However, in contrast to most compounds, **13** displayed a weak inhibition of hTS (IC_{50} 29 µM).

Compound **8** combined fragments of **3** and **7**. Due mainly to the tail ester, this modification improved the inhibition for both *Tb*PTR1 (IC_{50} 1 nM) and *Lm*PTR1 (IC_{50} 0.1 µM). The activity against *Tb*DHFR was similar to the N10-modified parent **3**, whereas *Lm*DHFR and hDHFR inhibition were again influenced by the tail modification (IC_{50} *Lm*DHFR **8**: 0.2 µM, **7**: 0.1 µM; hDHFR **8**: 13 µM, **7**: 12 µM). Compound **24** merged fragments of **3** and **23**. In *Tb*PTR1, this boosted the nanomolar IC_{50} of **23** to the picomolar range, while the activity towards *Lm*PTR1 remained similar to **23**. This can be related to the N10 ethyl, which seems disfavored in *Lm*PTR1 as judged by the modest inhibition of parent **3** (IC_{50} 13.3 µM).

Compounds **19** and **20** combined the scaffold of **16** with N10 modifications from **9** or **1**, respectively. Both compounds were nanomolar inhibitors of both PTR1 variants. The parent compounds, **9** and **1**, inhibited the parasite DHFR variants at micromolar to submicromolar levels, while **16** was inactive against all variants of DHFR. The combination with a favorable N10 substitution was able to restore medium micromolar anti-DHFR activity for the altered scaffold of parent **16** in the parasitic enzymes in **19** and **20**. Thus, specific combinations of the N10 and tail modifications allow a fine-tuning of the target inhibition profile for enzymes of specific parasite species.

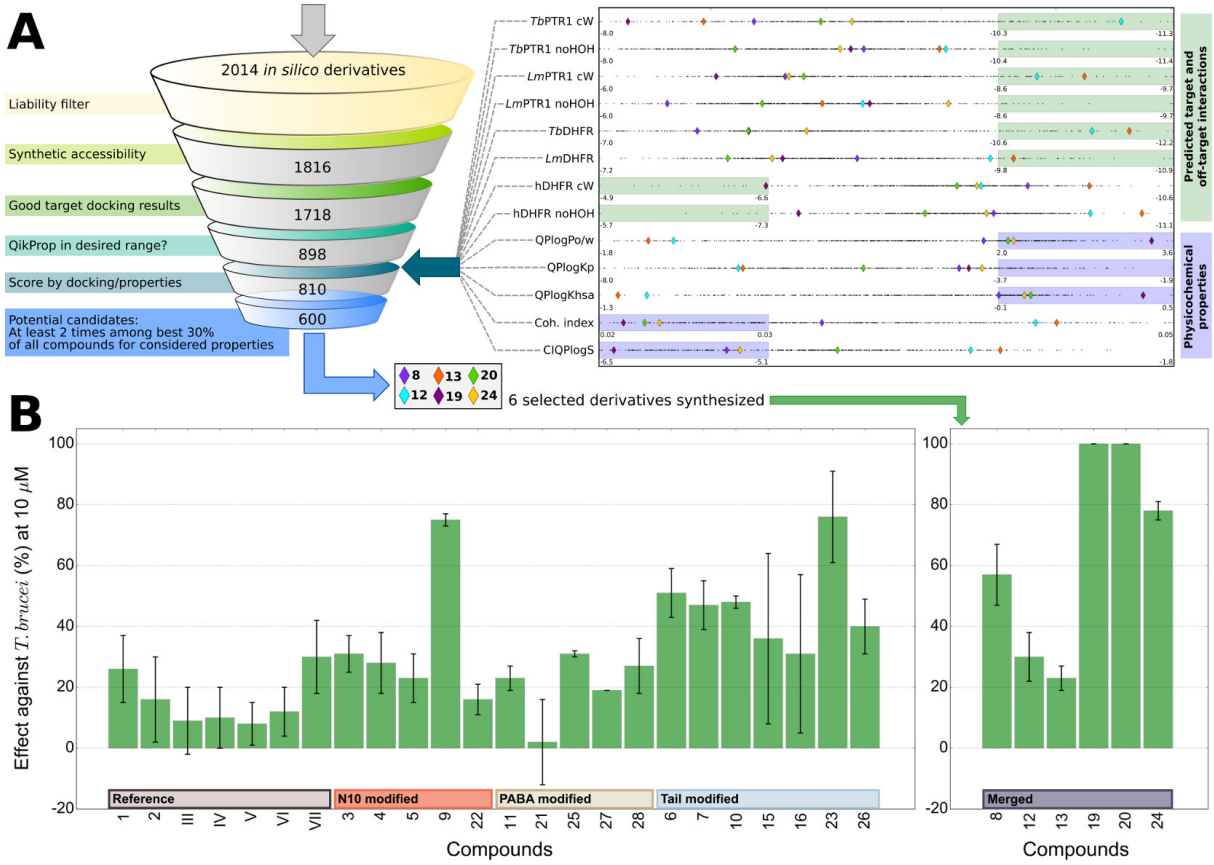

Figure 7. Workflow illustrating the prioritization of compounds in the *in silico* merged library (A) and anti-parasitic activity against *T. brucei* (B). (A) Compounds were filtered to reduce liabilities based on QikProp[39] results and the synthetically least accessible compounds as predicted with the Ambit-SA tool[40] were removed. As the next step, the compounds were filtered by the docking scores obtained for the different targets *Tb*PTR1, *Lm*PTR1, *Tb*DHFR and *Lm*DHFR, followed by evaluation of whether the QikProp properties that were found to correlate with anti-parasitic activity (QPLogPo/w: octanol-water partition coefficient; QPlogKp: skin permeability; QPlogKhsa: binding to human serum albumin; coh. index: Index of cohesive interaction in solids, (no. of hydrogen bond acceptors x no. of hydrogen bond donors x 0.5 / surface area)[41] and ClQPlogS: conformation-independent predicted aqueous solubility) were within the range typical for drug-like compounds. Finally, it was evaluated whether the compounds occurred at least twice among the best resulting 30% of compounds for each individual property, as indicated in the bar chart on the right-hand side by the green and blue regions for docking and QikProp results, respectively. All docking results are reported in kcal/mol. The aqueous solubility, S, is reported in mol dm^{-3}. For target docking, the best docking scores and for off-target docking, the worst docking scores were considered favorable. QikProp results were evaluated based on the correlation with the anti-parasitic activity, with high values for correlating (QPlogPo/w, QPlogKp, QPlogKhsa) and low values for anti-correlating properties (coh. index, ClQPlogS). The bar plot (right) shows the range of the final set of 600 candidate compounds with black dots reporting the individual values for every property. 6 representatives were selected for synthesis in the merged series, such that they span the covered property range, as indicated by the colored diamonds. (B) Percentage inhibition against *T. brucei brucei* for reference compounds and members of the N10-, PABA and tail-modified series (left) and the selected representatives of the *in silico* merged library (right). The average of at least three independent determinations is shown with the standard deviation. The inactive compounds in the tail modified series, **14**, **17** and **18** were omitted. Activities can be found in Table **S7**, SI.

The activity against *T. brucei* is related to the hydrophobicity of the compounds

We determined the anti-parasitic effect on *T. brucei brucei* Lister 427 bloodstream forms and *L. infantum* intramacrophage amastigotes (Figure **7B** and Table **S7**, SI). The pteridines were mostly inactive against *L. infantum* and, despite mostly being nanomolar inhibitors of *Tb*PTR1 and micromolar inhibitors of *Tb*DHFR, many of the new derivatives did not exceed 50% *T. brucei* inhibition at 10 μM compound concentration. Consistently, the multiple correlation coefficient between the *Tb*PTR1 and *Tb*DHFR IC_{50} values and the *T. brucei* bloodstream form

inhibition was R = 0.35 (equation **1**, SI) and indicated that the levels of target enzyme inhibition were only weakly correlated with the exhibited anti-parasitic effect when assuming a linear correlation. PTR1 inhibition alone showed a Pearson correlation of 0.34 with the *T. brucei* inhibition, while R was only 0.24 for DHFR inhibition, possibly because all compounds considered are much stronger inhibitors of PTR1 than DHFR.

To consider other factors affecting the anti-parasitic activity of the compounds, we computed the physicochemical properties and ADMET predictors of the reference and N10, PABA and tail-modified series compounds and assessed property correlations with the measured effect on *T. brucei*, see Table **1**. However, overall, only weak correlations of the individual properties with *T. brucei* inhibition were observed (Pearson R 0.47-0.55 and -0.41 – -0.54; R^2 0.17-0.30; computed as defined in the SI).

Table 1. Descriptors with significant correlations with the observed effect on *T. brucei* for the reference compounds and pteridines of the N10-, PABA- and tail modified series calculated with QikProp.[39] QPlogKp: Predicted skin permeability, log K_p; QPlogPo/w: Predicted octanol/water partition coefficient. QPlogKhsa: Prediction of binding to human serum albumin. Cohesive index: Index of cohesive interaction in solids, (no. of hydrogen bond acceptors x no. of hydrogen bond donors x 0.5 / surface area)[41]; ClQPlogS: Conformation-independent predicted aqueous solubility, log S with S in mol dm^{-3} being the concentration of the solute in a saturated solution that is in equilibrium with the crystalline solid. R (Pearson correlation) and R^2 were calculated using the percentage of inhibition of the *T. brucei brucei* Lister 427 bloodstream form at 10 µM compound concentration as defined in the SI. Only descriptors with at least a Pearson correlation/anti-correlation of 0.40/-0.40 and two-tailed P-values lower than the chosen significance level α of 0.05 are reported. Covered range: property values obtained for the currently considered compounds. Recommended range: values the properties take for typical drug-like molecules. Resampling recovery rate indicates in how many cases (expressed as percentage) the same property was identified when leaving a single compound out from the data set. The optimization direction indicates whether higher or lower values would putatively lead to improved anti-parasitic effects.

Predicted property	R	R^2	P value	Resampling recovery rate (%)	Covered range			Recommended range			Optimization direction
					Min	to	max	Min	to	max	
QPlogKp	0.55	0.30	0.003	100	-6.62	–	-3.60	-8.00	–	-1.00	↑
QPlogPo/w	0.49	0.24	0.010	96	-1.02	–	2.92	-2.00	–	6.50	↑
QPlogKhsa	0.47	0.22	0.010	96	-0.85	–	0.35	-1.50	–	1.50	↑
Cohesive index	-0.41	0.17	0.040	56	0.02	–	0.04	0.00	–	0.05	↓
ClQPlogS	-0.54	0.29	0.004	96	-6.71	–	-3.19	-6.50	–	0.50	↓

The strongest correlation was found for the predicted skin permeability, log Kp, as a descriptor linked to lipophilicity, with a Pearson R of 0.55 (R^2 0.30). The logPo/w and the binding to human serum albumin had slightly weaker correlations with the anti-parasitic effect (R: 0.49 R^2: 0.24 and R: 0.47 R^2: 0.22, respectively). For these properties, an increase in the value corresponds with higher anti-*T. brucei* activity. In contrast, some properties showed anti-correlation, for instance the aqueous solubility and the cohesive index[40] (R: -0.54 R^2: 0.29 and R: -0.41 R^2: 0.17, respectively). Taken together, all the data indicate an improved anti-parasitic effect with increased lipophilicity of the compounds.

We considered the correlating predicted properties as an additional prioritization filter for the *in silico* merged library, see Figure **7A**. Of the six synthesized compounds, **19**, **20** and **24** showed an improved percentage of *T. brucei* inhibition at 10 µM, as was suggested by their properties. For those compounds, EC_{50} values were determined, see Table **2**. Indeed, the three more lipophilic compounds were found to have low micromolar EC_{50}s against *T. brucei brucei* with **24** being the best (EC_{50} 0.66 ± 0.48 µM) and they showed SIs of 3-38 on the basis of their cytotoxicity on THP-1 derived macrophages.

Table 2. Properties with significant correlation with the observed effect on *T. brucei* for compounds in the merged series calculated with QikProp.[39] The properties are defined as in Table **1**. Values shown in bold face are within 90% of the previously determined top value or exceeded the previously obtained range for reference compounds and compounds in the N10-, PABA- and tail modified series, see Table **1**. The activity against *T. brucei brucei* Lister 427 bloodstream form at 10 µM compound concentration (%inhibition) is given. For the most promising compounds, **19**, **20** and **24**, in addition, measured EC_{50} values, No-observed-adverse-effect level (NOAEL), and Selectivity indeces are reported. EC_{50} and NOAEL represent the arithmetic average of at least two independent measurements done in triplicate. NOAEL was determined by cytotoxicity assessment on THP-1-derived macrophages by a colorimetric MTT (3-(4,5-dimethylthiazol-2-yl)-2,5-diphenyl tetrazolium bromide) assay, as previously reported.[42] N.D.: Not determined.

Compound	QP logKp	QP logPo/w	QP logKhsa	Cohesive index	CIQP logS	%inhibition of *T. brucei* at 10 µM ± SD	EC_{50} *T. brucei* [µM] ± SD	CC_{50} or NOAEL [µM]	Selectivity index (CC_{50} or lower limit / EC_{50})
8	-5.18	2.02	0.04	0.03	-5.32	57 ± 10	N.D.	N.D.	N.D.
12	-6.74	-1.16	0.05	0.04	-4.53	30 ± 8	N.D.	N.D.	N.D.
13	-6.48	-1.32	**0.43**	0.04	-6.35	23 ± 4	N.D.	N.D.	N.D.
19	-4.60	**3.36**	-1.23	**0.02**	-3.20	100 ± 0	4.53 ± 0.42	12.5 < CC_{50} < 25	3
20	-5.16	2.09	-1.14	**0.02**	-3.44	100 ± 0	1.30 ± 0.05	12.5 < CC_{50} < 25	10
24	**-3.91**	2.19	0.07	**0.02**	-5.43	78 ± 3	0.66 ± 0.48	25 < CC_{50} < 50	38
Pentamidine	N.D.	N.D.	N.D.	N.D.	N.D.	N.D.	0.0019 ± 0.0005	10	5263

Increased hydrophobicity often leads to liabilities

Potential liabilities were assessed by determining the inhibition of the *h*ERG potassium channel, five isoforms of CYP450 (1A2, 2C9, 2C19, 2D6 and 3A4), cytotoxicity against A459 cells (human lung adenocarcinoma epithelial cell line) and mitochondrial toxiticity against 786-O cells (renal carcinoma cell line) for all compounds at a concentration of 10 µM. The results are shown in Figure **8**. Further, the compounds passed a check for Pan-assay interference compounds (PAINS).

The reference compounds and the N10 series largely exhibited a safe profile. Aromatic modifications to the compound tail region, for instance in **27**, **17** and **20** (PABA, Tail and Merged series, respectively) were associated with notable *h*ERG liabilities. Increasing the hydrophobicity of the compounds further led to liabilities against some CYP isoforms, in particular, 2C9 and 2C19. The shortened tails of **25** and **27** resulted in a strong effect on CYP

isoform 2D6. Finally, several of the bulky, more hydrophobic compounds resulted in a cytostatic or cytotoxic effect on A549 cells, thus demonstrating a need for further optimization with increasing hydrophobicity being associated with greater liabilities.

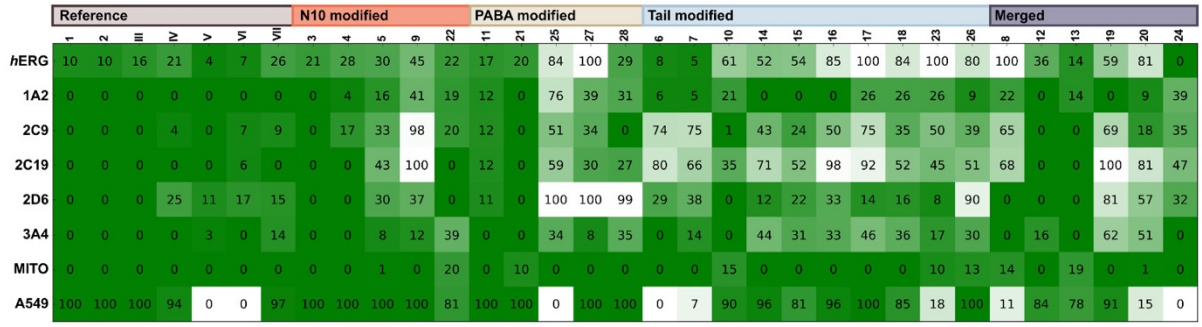

Figure 8. Heatmap representation of the liability assessment results. Inhibition of *h*ERG, five CYP isoforms (1A2, 2C9, 2C19, 2D6 and 3A4), mitochondrial toxicity (MITO) and growth inhibition of A549 cells were determined at 10 μM. The data are represented as percentages on a color scale from green (desired) to white (undesired value) with values reported in the map. For the inhibitory activities against *h*ERG, CYP isoforms and mitochondrial toxicity: green = 0%, white = 100% inhibition/toxicity, while for A549 cell growth inhibition green = 100% and white = 0% growth. The values are reported in Tables **S8,S9**.

In line with these observations, two of the best inhibitors of *T. brucei* bloodstream forms, **19** and **20** show 54% and 81% *h*ERG inhibition, respectively. **19** and, in many cases also **20,** also affected various CYP isoforms: 2C19 was inhibited to 100% and 81%, 2D6 to 81% and 57% and 3A4 to 62% and 51%, respectively. **19** further showed 69% CYP 2C9 inhibition. Finally, **20** was cytostatic with A549 cell growth reduced to 15% and **24** showed cytotoxicity, effectively completely inhibiting cell growth. Taken together, the most efficient inhibitors of *T. brucei* bloodstream forms were found to suffer from liabilities associated with their large hydrophobicity and require careful optimization of their cellular specificity.

Conclusion

Applying a multitarget-based approach to the development of novel therapies for HAT and leishmaniasis, we here focused on pteridine-based inhibitors of *L. major* and *T. brucei* PTR1 and DHFR and successfully designed the first known picomolar inhibitors of *Tb*PTR1. While *Lm*PTR1/*Lm*DHFR inhibition was previously explored for this compound class, we here demonstrated the potential of pteridine-based inhibitors against the *Tb*PTR1/*Tb*DHFR system.[27] We solved a crystal structure of the reference compound **1** bound to *Tb*PTR1 to confirm the overlap in observed binding modes between the two PTR1 variants and the preference of the inhibitor-like bound orientation in *Tb*PTR1. Guided by our detailed comparative study of on- and off-targets in the parasitic and human folate pathway[32], crystallographic reference structures and enzymatic evaluation of published reference pteridines[27,31], we designed 26 new pteridine derivatives that mostly have improved activity and selectivity. For their synthesis, we made use of an advanced MW-assisted protocol to improve the reaction yield of the pteroid step with reduced reaction time. Further determination

of crystal structures of complexes and computational docking enabled us to obtain a complete characterization of the binding modes of the pteridines to their molecular targets and supported the derivation of a SAR. The compounds were also tested against the human off-targets hDHFR and hTS. While they were sometimes only modestly selective for the parasitic DHFR variant, many showed 1000-fold and higher selectivities for PTR1 over the off-targets and thus, the novel PTR1 inhibitors can overall be considered selective for the parasite proteins.

While many compounds exhibited excellent inhibitory activity at the target level, they were often only modest inhibitors of *T. brucei brucei* bloodstream forms and inactive towards *L. infantum* intracellular amastigotes *in vitro*. We found that increased lipophilicity correlated with improved effects on *T. brucei*. We were able to prioritize compounds from an *in silico* library for synthesis by using predicted ADMET-related properties which suggested a likely improvement of the trypanocidal effect. In this way, we found three improved compounds,**19**, **20** and **24**, with low micromolar inhibition of *T. brucei brucei* (EC_{50} 0.66 – 4.53 μM). The result demonstrates that the approach employed here of combining property prediction correlation with multitarget-based compound design is a valuable approach to informing compound design, even when anti-parasitic data are available only as a percentage of inhibition determined at a single compound concentration. Further, integration of transport related considerations in the design[32], or using, for instance, structurally related scaffolds reported in the literature, which show inhibition of the *Leishmania* parasite, and a similar property-based correlation concept to that presented here, may help to overcome the current limitations of the pteridine-based compounds as inhibitors of intracellular parasites. Our data show that, overall, optimization for increased lipophilicity leads to more potent pteridine-based *T. brucei* inhibitors. However, increased lipophilicity can also introduce compound liabilities, e.g. for *h*ERG and CYPs. Strategies to avoid these, for instance by making use of a similar property-based optimization strategy, should thus be incorporated in future design efforts.

Experimental Procedures

General Synthesis Information. Reagent grade chemicals and solvents were purchased from commercial suppliers and used without further purification. Reactions were monitored by TLC on silica gel plates (Kieselgel 60, F254, Merck) and visualized using UV light, cerium ammonium sulphate or alkaline $KMnO_4$ aqueous solution. Solvents are abbreviated as follows: tetrahydrofuran (THF), ethyl ether (Et_2O), dimethyl sulfoxide (DMSO), dimethylacetamide (DMA), ethyl acetate (EtOAc), dichloromethane (DCM), dimethyl formamide (DMF), methanol (MeOH) and acetonitrile (ACN). The structures of the isolated compounds were confirmed by NMR spectroscopy and mass spectrometry. NMR spectra were recorded on Bruker 400 and 600 spectrometers with ^{1}H at 400.134 - 600 MHz and ^{13}C at 100.62 - 151 MHz. The purity of all synthesized

compounds was determined by elemental analyses performed on a PerkinElmer 240C instrument and by measurement of the melting point interval on a Stuart SMP3 instrument. Liquid chromatography−mass spectrometry (LC-MS) was used to obtain the molecular mass and analyze the purity of the products. The specifications of the LC-MS instrument were the following: Agilent 1200 HPLC coupled to a 6120 quadrupole mass spectrometer (ESI-API), UV detection at 254 and 210 nm, Agilent Zorbax XDB-18 C_{18} column (50 × 4.6 mm, 3.5 µm), gradient mobile phase consisting of MeOH/water/0.1% formic acid buffer, and a flow rate of 1.00 mL/min.

General synthetic procedure A: Reductive alkylation of amines using nitriles (32-33, 51, 74). After two vacuum/H_2 cycles to remove air from the reaction tube, the stirred mixture of the amine (1.0 equiv.), Pd\C catalyst (10 wt % of the amine), the respective RCN (5.0 equiv.) and NH_4OAc (1.0 equiv.) in MeOH (5.0 mL) was hydrogenated under ambient pressure (balloon) at room temperature for the appropriate time (24-36 h). The reaction mixture was filtrated using Celite cake before the filtrate was concentrated under reduced pressure. The residue was partitioned between Et_2O (10 mL) and water (10 mL). The aqueous phase was extracted thrice with Et_2O (10 mL), and the combined organic phases were washed with brine (10 mL), dried with anhydrous Na_2SO_4, filtered and concentrated under reduced pressure to yield the amines without further purification.

General synthetic procedure B: Amide coupling reaction for the synthesis of 27-28, 40-49, 52-54, 56-57, 71-72, 75. Carboxylic acid compounds (1 equiv.), EDC·HCl (1.1 equiv.) and HOBt (0.1 equiv.) were added to a dried round-bottomed flask and dissolved in DMF dry under N_2. The reaction mixture was cooled down to 0°C and stirred for 30 min before adding it to the respective amine (1 equiv.) with/without TEA (2−3 equiv.). After stirring overnight at rt (room temperature), the mixture was washed 1x with saturated $NaHCO_3$, 1x with H_2O and 1x with brine. The washed organic mixture was then dried with Na_2SO_4, concentrated in vacuo and purified using column chromatography (SiO_2, eluent: Cy/EtOAc or DCM/MeOH or DCM/EtOAc/MeOH) to give the desired amide.

General synthetic procedure C: MW alkylation 1-26. To a suspension of amine intermediates (1 equiv.) in DMA (3 mL) in a microwave Biotage vial, **29** (1.2 equiv.), K_2CO_3 (3 equiv.) and KI (0.1 equiv.) were added. The vial was sealed and heated by microwave irradiation in a Biotage® Initiator+ microwave at 60°C for 20 min (30' for compounds **23**-**25**), before cooling to room temperature and diluting with water (20 mL).

The precipitate was then collected by filtration and dried before the final compound was purified by fractional crystallization from methanol, DCM and Et_2O.

General synthetic procedure D: S_NAr for the preparation of 4-substituted benzaldehyde (63-65). A mixture of substituted phenol **58**-**60** (1 equiv.), 4-fluorobenzaldehyde (1 equiv.), and K_2CO_3 (3 equiv.) in DMF (10 mL) was refluxed for 16–18 h under nitrogen. After cooling, the solution was concentrated *in vacuo* to give a crude residue, which was purified by crystallization in 1N $NaHCO_3$. The obtained crystal was washed with H_2O to obtain the desired benzaldehyde derivatives.

General synthetic procedure E: Preparation of primary amines from 4-substituted benzaldehyde (66-68). A solution of carbonyl (aldehyde) compounds **66**-**68** (1 equiv.) and hydroxylammonium chloride (1.2 equiv.) in ethanol (30 mL) was stirred for 1h at rt. Subsequently, 12 M hydrochloric acid (4 equiv.) and zinc dust (2.5 equiv.) were slowly added to the solution and let to stir at rt for 15 min. To the resulting slurry, a solution of ammonia (30%, 14 mL) and sodium hydroxide (6 M, 30 mL) was added dropwise and the mixture was stirred at rt for another 15 min. Then, the resulting solution was extracted with DCM, dried over anhydrous Na_2SO_4, and filtered. The solvent was removed under vacuum to give the amines without further purification.

Protein expression and purification. Recombinant *Tb*PTR1, *Lm*PTR1, *Tb*DHFR-TS, *Lm*DHFR-TS, hDHFR and hTS were expressed and purified according to previously reported procedures.[26,42,43]

Crystallization of *Tb*PTR1 and *Lm*PTR1. Well-ordered monoclinic crystals of histidine-tagged *Tb*PTR1 were obtained by the vapor diffusion hanging drop technique at rt.[44] Drops were prepared by mixing equal volumes of protein and precipitant solution (2 - 2.5 M sodium acetate and 0.1 M sodium citrate pH 5) according to a previously described procedure.[42] The *Tb*PTR1–cofactor–inhibitor ternary complexes were obtained by the soaking technique. The compounds, solubilized in DMSO, were diluted in the cryoprotectant solution (30% vol/vol glycerol added to the precipitant solution) to a final concentration of 2-4 mM (keeping the DMSO concentration below 10% vol/vol). Crystals were then transferred in the resulting soaking/cryoprotectant solution and flash frozen in liquid nitrogen after 8-24 h exposure.

Crystals of *Lm*PTR1 were prepared as described elsewhere.[38] The *Lm*PTR1–cofactor–**4** ternary complex was obtained by the soaking technique, adding 2 mM compound (solubilized in DMSO, without exceeding the 10% drop volume) directly into the

crystallization drop. After 5 h, crystals were transferred to the cryoprotectant solution and flash frozen in liquid nitrogen.

Data collection, structure solution and refinement. X-ray crystallographic data were collected using synchrotron radiation at the Diamond Light Source (DLS, Didcot, United Kingdom) beamlines I04-1 and I03 equipped with a Dectris Pilatus 6M-F and a Pilatus3 6M detector, respectively. Reflections were integrated using MOSFLM and scaled with Scala (CCP4 suite).[45-49] Data collection and processing statistics are reported in Table **S2**. The crystals of *Tb*PTR1 and *Lm*PTR1 belonged to the primitive monoclinic space group $P2_1$ and the primitive orthorhombic space group $P2_12_12_1$, respectively. Both had a functional enzyme tetramer in the asymmetric unit. The structures were solved by molecular replacement using MOLREP and either a *Tb*PTR1 (PDB-ID 5jdc) or a *Lm*PTR1 tetramer (PDB-ID 5l4n) as the searching model (all non-protein atoms were excluded).[38,42,50] Models were refined using REFMAC5 (CCP4 suite).[51] Visual inspection and manual rebuilding of missing atoms was performed using Coot.[52,53] Water molecules were added with the automated standard procedures implemented in the software ARP/wARP and checked with Coot.[54] In the higher resolution complexes of *Tb*PTR1 with compounds **3** and **4**, all atoms were refined anisotropically in the final refinement cycles and hydrogen atoms were added in the calculated positions. The occupancies of exogenous ligands were individually adjusted to values resulting in atomic displacement parameters comparable to those of surrounding protein atoms in fully occupied sites. The final models were checked with Coot and Procheck.[55] Statistics for data refinement are reported in Table **S3**. Figures were generated using CCP4mg.[56] Coordinates and structure factors were deposited in the Protein Data Bank under the PDB-IDs 6rx5 (*Tb*PTR1-NADPH/$NADP^+$-**1**), 6rx0 (*Tb*PTR1-NADPH/$NADP^+$-**3**), 6rx6 (*Tb*PTR1-NADPH/$NADP^+$-**4**), and 6rxc (*Lm*PTR1-NADPH/$NADP^+$-**4**).

***Tb*PTR1, *Tb*DHFR, *Lm*PTR1, *Lm*DHFR, hDHFR and hTS target/off-target enzyme assays.** *In vitro* assays for *Tb*PTR1 and *Lm*PTR1 were based on the coupled assay reported by Shanks et al.[57] The assay non-enzymatically links the reduction of cytochrome c (Cc) with the reduction of dihydrobiopterin to tetrahydrobiopterin, catalyzed by PTR1. The formation of reduced Cc (Fe^{2+}) results in a signal increase in the photometric readout at 550 nm wavelength. *Tb*PTR1 and *Lm*PTR1 assays were performed in a buffer containing 20 nM sodium citrate (pH 6.0) in a well-plate-based format as previously reported.[42] *Lm*DHFR, *Tb*DHFR, hDHFR and hTS activities were assessed spectrophotometrically according to published procedures.[58,59] Each inhibitory

compound was assayed at five different concentrations in duplicate (confidence interval $\rho < 0.05$) and IC_{50} values were calculated as described in the SI.

Computational preparation of pteridine compounds and protein receptors and SiteMap calculation of DHFR pocket volumes. The three-dimensional structures of the compounds were created from SMILES strings and optimized with the OPLS_2005 force field using LigPrep of Maestro (Schrödinger, LLC) as described previously, except that tautomers were created for the pH range 5.0-8.0 and both an N1-deprotonated and an N1-protonated tautomer was considered for every compound.[42,60-63] In addition, all different substituents to the N10 position, PABA modifications and compound tail alterations present in reference compounds, compounds of the N10-, PABA- or tail-modified series were combined in all possible permutations *in silico* in a 'merged' series and prepared similarly.

All receptors were prepared in the presence of MTX (from the following PDB-IDs for *Tb*PTR1: 2c7v, *Lm*PTR1: 1e7w, *Tb*DHFR and *Lm*DHFR: 3cl9 and hDHFR: 1u72) to improve the interactions of binding site residues and the conserved water molecules with the pteridine core of the compounds. Receptor preparation was carried out following published procedures with minor modifications.[42,60,61,64-66] For the *Lm*PTR1 (PDB-ID 1e92) and *Tb*PTR1 (PDB-ID 2x9g) receptors, an energy minimization with a harmonic restraint of 25 kcal mol^{-1} $Å^{-2}$ on heavy atoms and no restraint on hydrogens was performed until the heavy atom RMSD relative to the previous minimization step was less than 0.30 Å.[67] For the *Tb*DHFR receptor, PDB-ID 3rg9 was used; for *Lm*DHFR, our previously published homology model based on a *Tc*DHFR-TS template (PDB-ID 3inv) was chosen.[32] For off-target docking, we used the hDHFR structure 1u72. For PTR1, we also considered the previously described set of conserved water molecules as identified by the WatCH clustering approach.[42,64] Further, using WatCH, we identified conserved water sites in hDHFR in a similar approach as described in the SI.[64] Except for the parasite DHFR variants, where the identification of a conserved water set was not possible, all receptors were prepared both with the identified set of conserved structural waters and without explicit water molecules.

Grid preparation was done as described before for *Lm*PTR1 and *Tb*PTR1[42] with the following grid centers and rotatable groups: (i) *Lm*PTR1: center Phe113, rotatable OH in Ser111, Thr184, Tyr191, Tyr194, Thr195, Tyr283 and $NADP^+$ ribose; (ii) *Tb*PTR1: center Phe97, rotatable OH/SH in Ser95, Cys168, Tyr174 and $NADP^+$ ribose; (iii) *Lm*DHFR: center Phe31, rotatable OH/SH in Thr35, Thr36, Ser61, Cys130, Tyr137, Thr155, $NADP^+$ ribose; (iv) *Tb*DHFR: center Phe58, rotatable OH in Thr46, Thr62, Thr86, Ser89, Ser98, Tyr166, Thr184, $NADP^+$ ribose; and (v) hDHFR: center Phe34, rotatable OH in Thr38, Thr39, Ser59, Tyr121, $NADP^+$ ribose.

The volumes of the binding pockets of *Tb*DHFR (PDB-ID 3rg9), hDHFR (1u72) and the *Lm*DHFR homology model were computed with Schrödinger SiteMap[60,68,69] as described in the SI.

Computational docking studies. Docking studies were performed using a rigid receptor in Glide standard precision (SP) and extra precision (XP) modes and employing the Induced Fit (IF) protocol to allow for refinement of binding site residues.[60,70-76] For rigid receptor docking, van der Waals radii scaling of ligand atoms and settings for sampling, consideration of Epik state penalties in the docking score, rewarding of intramolecular hydrogen bonds and enhancement of the planarity of conjugated π-groups were chosen as described previously[42], but a total of 50 poses per ligand were subjected to post-docking energy minimization. For the *in silico* library, we used SP docking with a constraint on all heavy atoms of the pteridine core to match the orientation of MTX in the corresponding protein receptor with a tolerance of 1 Å.

In addition, since some compounds showed major variation in substituent size when compared to the starting scaffold and explicit water molecules are treated as frozen in the standard SP/XP docking, we performed additional studies allowing protein side chain and water reorganization in response to ligand binding: We used the IF workflow implemented in Maestro with the standard protocol. The planarity of conjugated π-groups was enhanced and a Prime refinement was performed for residue side chains within 5 Å of ligand atoms. XP redocking was done as previously described, yielding up to 20 receptor-ligand complexes per compound.[42]
The validation of the chosen docking protocol is presented in the SI.

Computational property prediction, Pan-assay interference compounds (PAINS) and correlation analysis with anti-parasitic data. Physico-chemical descriptors and parameters related to ADMET were computed for all prepared compounds using QikProp (Schrödinger).[39] We then used Python scripts and SciPy to compute Pearson correlations (R), R^2 values and two-tailed P-values for each property with the measured percentage of inhibition of *T. brucei* at 10 µM compound concentration. Only properties with a statistical significance level α no more than 0.05 were considered further. To ensure robustness against leaving single compounds out of the analysis, we performed an additional resampling analysis by leaving every compound out once before recomputing the correlations. Properties with R above 0.40 or below -0.40, P-value $\leq$ 0.05 and being identified in more than 50% of the resampling correlation analyses were considered to be the most robust markers for the optimization for anti-parasitic effect. These properties were employed to prioritize compounds for synthesis as part of series 4 as demonstrated in Figure **7** and explained in detail in the SI.

In addition, a multivariate correlation coefficient between parasite target protein inhibition and anti-parasitic activity was determined. Details on the correlation calculations are reported in the SI.

Finally, all synthesized compounds were checked for PAINS (PAINS filters A, B and C), undesirable substructure moieties, covalent inhibition, and compliance with the rule-of-five with the FAF-Drugs4 webserver (fafdrugs4.mti.univ-paris-diderot.fr/) by inputing SMILES strings for the compounds.[77]

***In vitro* biological evaluation against *T. brucei and L. infantum* intramacrophage amastigotes.** The efficacy against *T. brucei brucei* Lister 427 bloodstream forms was evaluated in a modified resazurin-based assay as previously described.[78] Cells were grown at 37°C and 5% CO_2 in a complete HMI-9 medium supplemented with 10% fetal calf serum (FCS) and 100 UI/mL of penicillin/streptomycin. Cultures were then diluted to a cell density of 2×10^6 /mL. For the assay, compounds were prepared in 10 mM DMSO and diluted in HMI-9 to a 40 µM solution (0.4% DMSO). The assay solution was further used to perform serial dilutions (1:2) in a 96-well plate. Mid-log bloodstream forms (100 µL) were added in complete HMI-9 medium at a final cell density of 1×10^4 /mL in a well volume of 200 µL after compound addition, leading to a maximum DMSO concentration of 0.2%. Following incubation for 72 h at 37°C and 5% CO_2, 20 µL of 0.5 mM resazurin solution were added and plates were further incubated for 4 h under similar conditions. Fluorescence was then measured using a Synergy 2 multi-mode reader (BioTek) at 540 and 620 nm excitation and emission wavelength, respectively. The efficacy of compounds against *L. infantum* intracellular amastigotes was determined according to Sereno et al. with slight modifications described in detail in the SI.[79]

Liability assays. The *h*ERG cardiotoxicity assay was performed using the Invitrogen Predictor *h*ERG fluorescence polarization (FP) assay. A membrane fraction containing *h*ERG (Predictor *h*ERG membrane) was used together with a red fluorescent high-affinity ligand of the *h*ERG channel (Predictor *h*ERG Tracer Red). Displacement of the latter from *h*ERG by binding of the test compound can be determined in a FP-based format.[42]

Cytochrome P450 (CYP450) assays against isoforms 1A2, 2C9, 2C19, 2D6 and 3A4 were performed using the Promega P450-Glo assay platform. Microsomal preparations of cytochrome P450s from baculovirus-infected insect cells were used. In this assay, light is generated when a CYP450 enzyme acts on its substrate and a decrease thereof was indicative of inhibitory effects of the tested compound on the respective isoform.[42]

For monitoring mitochondrial toxicity caused by the test compounds in the 786-O cell line, uptake of MitoTracker Red (chloromethyl-X-rosamine) combined with high content

imaging was used. Cells were maintained in Rosswell Park Memorial Institute (RPMI)-1640 medium containing 2 mM glutamine, FCS (10% v/v), streptomycin (100 µg/mL), and penicillin G (100 U/mL).[42]

The cytotoxicity assay against A549 cells was performed using the CellTiter-Glo assay from Promega. The number of viable cells present is directly proportional to the cellular ATP content, which is detected. The A549 cells were obtained from DSMZ (German Collection of Microorganisms and Cell Cultures, Braunschweig, Germany) and grown in Dulbecco's modified Eagle medium (DMEM) with FCS (10% v/v), streptomycin (100 µg/mL) and penicillin G (100 U/mL).[42]

Supplemental Information

Supplemental Figures **S1**-**8**, Supplemental Tables **S1**-**12**, Supplemental experimental procedures and compound characterization.

Additional supplementary data are freely available at https://fairdomhub.org/investigations/417: QikProp prediction results for synthesized and *in silico* pteridines and corresponding SOP. PAINS filtering results, Python modules for correlating QikProp data with experimental activities and for computing a multiple correlation between target and parasite inhibition. Compound library construction data and SOP, prepared docking receptors (PDB) with SOP, all Glide XP rigid-body docking results as PDB-files of the receptor-ligand complexes and SOP as well as selected discussed induced fit docking results and corresponding SOP.

PDB-Codes

Crystal structures described in this paper are available in the Protein Data Bank with identifiers: 6rx5 (*Tb*PTR1-NADPH/$NADP^+$-**1**), 6rx0 (*Tb*PTR1-NADPH/$NADP^+$-**3)**, 6rx6 (*Tb*PTR1-NADPH/$NADP^+$-**4**), 6rxc (*Lm*PTR1-NADPH/$NADP^+$-**1**).

Corresponding author information

* Email: mariapaola.costi@unimore.it (M.P.C.), a.venturelli@tydockpharma.com (A.V.), rebecca.wade@h-its.org (R.C.W.)

Author Contributions

† These authors contributed equally and are considered as first co-authors. Conceptualization, M.P.C., A.V., R.C.W.; Computational Methodology and Investigation, I.P., J. P.-H.; Chemical synthesis Methodology and Investigation, A.Q.; Enzyme assay Methodology and Investigation,

R.L., M.S., P.L.; Crystallography Methodology and Investigation, G.L., F.D.P., L.D.I., C.P.; ADMET Methodology and Investigation, S.G., G.W., B.E., M.K.; Parasite assay Methodology and Investigation, N.S.; Writing – Original Draft, I.P., Writing – Review & Editing, I.P., M.P.C., R.C.W.; Supervision, S.M., A.C.S., M.P.C, A.V., R.C.W.

Notes

The authors declare no competing interests.

Acknowledgements

This work has received funding from the European Union's Seventh Framework Programme for research, technological development, and demonstration under grant agreement no. 603240 (NMTrypI, New Medicines for Trypanosomatidic Infections, https://fp7-nmtrypi.eu/). We thank Prof. Antonio Carta, University of Sassari, for providing the reference compounds **III**-**VII**. I.P., J.P.-H. and R.C.W. gratefully acknowledge the support of the Klaus Tschira Foundation. J.P.-H. acknowledges support from the Polish National Science Centre (grant no. 2016/21/D/NZ1/02806) and the BIOMS program at the Interdisciplinary Center for Scientific Computing (IWR), Heidelberg University.

Abbreviations used

DHFR: Dihydrofolate reductase; HAT: Human African Trypanosomiasis; MTX: Methotrexate; NTDs: Neglected Tropical Diseases; PABA: *para*-amino benzoic acid; PAINS: Pan-Assay Interference compounds; PTR1: Pteridine reductase 1; SI: Selectivity index; TS: Thymidylate synthase

References

1. Neglected tropical diseases. https://www.who.int/neglected_diseases/en/ (accessed May 2020).
2. The WHO Strategic and Technical Advisory Group for Neglected Tropical Diseases (WHO STAG). https://www.who.int/neglected_diseases/diseases/Adoption_additional_NTDs.pdf?ua=1,%202017.
3. Barrett, M. P., Burchmore, R. J. S., Stich, A., Lazzari, J. O., Frasch, A. C., Cazzulo, J. J., Krishna, S. The trypanosomiases. *Lancet*. **2003** *362*, 1469–1480.
4. Blum, J., Schmid, C., Burri, C. Clinical aspects of 2541 patients with second stage human African trypanosomiasis. *Acta Trop.* **2006** *97*, 55–64.
5. Stuart, K., Brun, R., Croft, S., Fairlamb, A., Gürtler, R. E., McKerrow, J., Reed, S., Tarleton, R. Kinetoplastids: related protozoan pathogens, different diseases. *J. Clin. Invest.* **2008** *118*, 1301–1310.
6. Cunningham, A. C. Parasitic adaptive mechanisms in infection by *Leishmania*. *Exp. Mol. Pathol.* **2002** *72*, 132–141.
7. Herwaldt, B. L. Leishmaniasis. *Lancet.* **1999** *354*, 1191–1199.
8. Castillo, E., Dea-Ayuela, M. A., Bolás-Fernández, F., Rangel, M., González-Rosende, M.

E. The kinetoplastid chemotherapy revisited: current drugs, recent advances and future perspectives. *Curr. Med. Chem.* **2010** *17*, 4027–4051.
9. Machado-Silva, A., Goulart Guimarães, P. P., Pereira Tavares, C. A., Sinisterra, R. D. New perspectives for leishmaniasis chemotherapy over current anti-leishmanial drugs: a patent landscape. *Expert Opin. Ther. Pat.* **2015** *25*, 247–260.
10. Gilbert, I. H. Drug discovery for neglected diseases: molecular target-based and phenotypic approaches. *J. Med. Chem.* **2013** *56*, 7719-7726.
11. Müller, J., Hemphill, A. Drug target identification in protozoan parasites. *Expert Opin. Drug Discov.* **2016** *11*, 815-824.
12. Borsari, C., Quotadamo, A., Ferrari, S., Venturelli, A., Cordeiro-da-Silva, A., Santarem, N., Costi, M. P. Chapter Two - Scaffolds and biological targets avenue to fight against drug resistance in leishmaniasis. *Annu. Rep. Med. Chem.* **2018** *51*, 39-95.
13. Shuvalov, O., Petukhov, A., Daks, A., Fedorova, O., Vasileva, E., Barlev, N. A. One-carbon metabolism and nucleotide biosynthesis as attractive targets for anticancer therapy. *Oncotarget* **2017** *8*, 23955–23977.
14. Anderson, A. C., Wright, D. L. Antifolate agents: a patent review (2010 - 2013). *Expert Opin. Ther. Pat.* **2014** *24*, 687–697.
15. Hawser, S., Lociuro, S., Islam, K. Dihydrofolate reductase inhibitors as antibacterial agents. *Biochem. Pharmacol.* **2006** *71*, 941–948.
16. Yuthavong, Y., Yuvaniyama, J., Chitnumsub, P., Vanichtanankul, J., Chusacultanachai, S., Tarnchompoo, B., Vilaivan, T., Kamchonwongpaisan, S. Malarial (*Plasmodium falciparum*) dihydrofolate reductase-thymidylate synthase: structural basis for antifolate resistance and development of effective inhibitors. *Parasitology* **2005** *130*, 249–259.
17. Christensen, K. E., MacKenzie, R. E. Mitochondrial one-carbon metabolism is adapted to the specific needs of yeast, plants and mammals. *Bioessays* **2006** *28*, 595–605.
18. Cullia, G., Tamborini, L., Conti, P., De Micheli, C., Pinto, A. Folates in *Trypanosoma brucei*: Achievements and opportunities. *ChemMedChem* **2018** *13*, 2150–2158.
19. Bello, A. R., Nare, B., Freedman, D., Hardy, L., Beverley, S. M. PTR1: A reductase mediating salvage of oxidized pteridines and methotrexate resistance in the protozoan parasite *Leishmania major*. *Proc. Natl. Acad. Sci. U. S. A.* **1994** *91*, 11442–11446.
20. Dawson, A., Gibellini, F., Sienkiewicz, N., Tulloch, L. B., Fyfe, P. K., McLuskey, K., Fairlamb, A. H., Hunter, W. N. Structure and reactivity of *Trypanosoma brucei* pteridine reductase: inhibition by the archetypal antifolate methotrexate. *Mol. Microbiol.* **2006** *61*, 1457–1468.
21. Vickers, T. J., Beverley, S. M. Folate metabolic pathways in *Leishmania*. *Essays Biochem.* **2011** *51*, 63–80.
22. Ong, H. B., Sienkiewicz, N., Wyllie, S., Fairlamb, A. H. Dissecting the metabolic roles of pteridine reductase 1 in *Trypanosoma brucei* and *Leishmania major*. *J. Biol. Chem.* **2011** *286*, 10429–10438.
23. Sienkiewicz, N., Ong, H. B., Fairlamb, A. H. *Trypanosoma brucei* pteridine reductase 1 is essential for survival in vitro and for virulence in mice. *Mol. Microbiol.* **2010** *77*, 658–671.
24. Mpamhanga, C. P., Spinks, D., Tulloch, L. B., Shanks, E. J., Robinson, D. A., Collie, I. T., Fairlamb, A. H., Wyatt, P. G., Frearson, J. A., Hunter, W. N., Gilbert, I. H., Brenk, R. One scaffold, three binding modes: Novel and selective pteridine reductase 1 inhibitors derived from fragment hits discovered by virtual screening. *J. Med. Chem.* **2009** *52*, 4454–4465.
25. Spinks, D., Ong, H. B., Mpamhanga, C. P., Shanks, E. J., Robinson, D. A., Collie, I. T., Read, K. D., Frearson, J. A., Wyatt, P. G., Brenk, R., Fairlamb, A. H., Gilbert, I. H. Design, synthesis and biological evaluation of novel inhibitors of *Trypanosoma brucei* pteridine reductase 1. *ChemMedChem* **2011** *6*, 302–308.
26. Cavazzuti, A., Paglietti, G., Hunter, W. N., Gamarro, F., Piras, S., Loriga, M., Allecca, S., Corona, P., McLuskey, K., Tulloch, L., Gibellini, F., Ferrari, S., Costi, M. P. Discovery of potent pteridine reductase inhibitors to guide antiparasite drug development. *Proc. Natl. Acad. Sci. U. S. A.* **2008** *105*, 1448–1453.
27. Ivanetich, K. M., Santi, D. V. Bifunctional thymidylate synthase-dihydrofolate reductase in protozoa. *FASEB J.* **1990** *4*, 1591–1597.

28. Schormann, N., Senkovich, O., Walker, K., Wright, D. L., Anderson, A. C., Rosowsky, A., Ananthan, S., Shinkre, B., Velu, S., Chattopadhyay, D. Structure-based approach to pharmacophore identification, *in silico* screening, and three-dimensional quantitative structure-activity relationship studies for inhibitors of *Trypanosoma cruzi* dihydrofolate reductase function. *Proteins* **2008** *73*, 889–901.
29. Schormann, N., Velu, S. E., Murugesan, S., Senkovich, O., Walker, K., Chenna, B. C., Shinkre, B., Desai, A., Chattopadhyay, D. Synthesis and characterization of potent inhibitors of *Trypanosoma cruzi* dihydrofolate reductase. *Bioorg. Med. Chem.* **2010** *18*, 4056–4066.
30. Corona, P., Gibellini, F., Cavalli, A., Saxena, P., Carta, A., Loriga, M., Luciani, R., Paglietti, G., Guerrieri, D., Nerini, E., Gupta, S., Hannaert, V., Michels, P. A. M., Ferrari, S., Costi, P. M. Structure-based selectivity optimization of piperidine-pteridine derivatives as potent *Leishmania* pteridine reductase inhibitors. *J. Med. Chem.* **2012** *55*, 8318–8329.
31. Panecka-Hofman, J., Pöhner, I., Spyrakis, F., Zeppelin, T., Di Pisa, F., Dello Iacono, L., Bonucci, A., Quotadamo, A., Venturelli, A., Mangani, S., Costi, M. P., Wade, R. C. Comparative mapping of on-targets and off-targets for the discovery of anti-trypanosomatid folate pathway inhibitors. *Biochim. Biophys. Acta, Gen. Subj.* **2017** *1861*, 3215–3230.
32. Tulloch, L. B., Martini, V. P., Iulek, J., Huggan, J. K., Lee, J. H., Gibson, C. L., Smith, T. K., Suckling, C. J., Hunter, W. N. Structure-based design of pteridine reductase inhibitors targeting African sleeping sickness and the leishmaniases. *J. Med. Chem.* **2010** *53*, 221–229.
33. Quotadamo, A., Linciano, P., Costi, M. P., Venturelli, A. Optimization of *N*-alkylation in the synthesis of methotrexate and pteridine-based derivatives under microwave-irradiation. *ChemistrySelect* **2019** *4*, 4429–4433.
34. Sajiki, H., Ikawa, T., Hirota, K. Reductive and catalytic monoalkylation of primary amines using nitriles as an alkylating reagent. *Org. Lett.* **2004** *6*, 4977–4980.
35. Ikawa, T., Fujita, Y., Mizusaki, T., Betsuin, S., Takamatsu, H., Maegawa, T., Monguchia, Y., Sajiki, H. Selective N-alkylation of amines using nitriles under hydrogenation conditions: facile synthesis of secondary and tertiary amines. *Org. Biomol. Chem.* **2012** *10*, 293–304.
36. Ayedi, M. A., Le Bigot, Y., Ammar, H., Abid, S., El Gharbi, R., Delmas, M. Synthesis of primary amines by one-pot reductive amination of aldehydes. *Synth. Commun.* **2013** *43*, 2127-2133.
37. Gourley, D. G., Schüttelkopf, A. W., Leonard, G. A., Luba, J., Hardy, L. W., Beverley, S. M., Hunter, W. N. Pteridine reductase mechanism correlates pterin metabolism with drug resistance in trypanosomatid parasites. *Nat. Struct. Biol.* **2001** *8*, 521–525.
38. Di Pisa, F., Landi, G., Dello Iacono, L., Pozzi, C., Borsari, C., Ferrari, S., Santucci, M., Santarem, N., Cordeiro-da-Silva, A., Moraes, C. B., Alcantara, L. M., Fontana, V., Freitas-Junior, L. H., Gul, S., Kuzikov, M., Behrens, B., Pöhner, I., Wade, R. C., Costi, M. P., Mangani, S. Chroman-4-one derivatives targeting pteridine reductase 1 and showing anti-parasitic activity. *Molecules* **2017** *22*, 426.
39. Schrödinger, LLC, New York, NY, Schrödinger Release 2015-4, **2015**, QikProp v4.6.
40. AMBIT. (**2018**). Ambit-SA (SyntheticAccessibilityCli), http://ambit.sourceforge.net/reactor.html (accessed October 2020).
41. Jorgensen, W. L., Duffy, E. M. Prediction of drug solubility from Monte Carlo simulations. *Bioorg. Med. Chem. Lett.* **2000** *10*, 1155–1158.
42. Borsari, C., Luciani, R., Pozzi, C., Poehner, I., Henrich, S., Trande, M., Cordeiro-da-Silva, A., Santarem, N., Baptista, C., Tait, A., Di Pisa, F., Dello Iacono, L., Landi, G., Gul, S., Wolf, M., Kuzikov, M., Ellinger, B., Reinshagen, J., Witt, G., Gribbon, P., Kohler, M., Keminer, O., Behrens, B., Costantino, L., Tejera Nevado, P., Bifeld, E., Eick, J., Clos, J., Torrado, J., Jiménez-Antón, M. D., Corral, M. J., Alunda, J. M., Pellati, F., Wade, R. C., Ferrari, S., Mangani, S., Costi, M. P. Profiling of flavonol derivatives for the development of antitrypanosomatidic drugs. *J. Med. Chem.* **2016** *59*, 7598–7616.
43. Cardinale, D., Guaitoli, G., Tondi, D., Luciani, R., Henrich, S., Salo-Ahen, O. M., Ferrari, S., Marverti, G., Guerrieri, D., Ligabue, A., Frassineti, C., Pozzi, C., Mangani, S., Fessas, D., Guerrini, R., Ponterini, G., Wade, R. C., Costi, M. P. Protein-protein interface-binding

peptides inhibit the cancer therapy target human thymidylate synthase. *Proc. Natl. Acad. Sci. U. S. A.* **2011** *108*, E542–E549.
44. Benvenuti, M., Mangani, S. Crystallization of soluble proteins in vapor diffusion for X-ray crystallography. *Nat. Protoc.* **2007** *2*, 1633-1651.
45. Battye, T. G. G., Kontogiannis, L., Johnson, O., Powell, H. R., Leslie, A. G. W. *iMOSFLM*: a new graphical interface for diffraction-image processing with *MOSFLM*. *Acta Crystallogr.* **2011** *67*, 271–281.
46. Powell, H. R., Johnson, O., Leslie, A. G. W. Autoindexing diffraction images with *iMosflm*. *Acta Crystallogr.* **2013** *69*, 1195–1203.
47. Evans, P. Scaling and assessment of data quality. *Acta Crystallogr.* **2006** *62*, 72–82.
48. Evans, P. An introduction to data reduction: space-group determination, scaling and intensity statistics. *Acta Crystallogr.* **2011** *67*, 282–292.
49. CCP4. The CCP4 suite: programs for protein crystallography. *Acta Crystallogr.* **1994** *50*, 760–763.
50. Vagin, A., Teplyakov, A. Molecular replacement with *MOLREP*. *Acta Crystallogr.* **2010** *66*, 22–25.
51. Murshudov, G. N., Skubák, P., Lebedev, A. A., Pannu, N. S., Steiner, R. A., Nicholls, R. A., Winn, M. D., Long, F., Vagin, A. A. *REFMAC5* for the refinement of macromolecular crystal structures. *Acta Crystallogr.* **2011** *67*, 355–367.
52. Emsley, P., Cowtan, K. *Coot*: model-building tools for molecular graphics. *Acta Crystallogr.* **2004** *60*, 2126–2132.
53. Emsley, P., Lohkamp, B., Scott, W. G., Cowtan, K. Features and development of *Coot*. *Acta Crystallogr.* **2010** *66*, 486–501.
54. Langer, G. G., Cohen, S. X., Lamzin, V. S., Perrakis A. Automated macromolecular model building for X-ray crystallography using ARP/wARP version 7. *Nat. Protoc.* **2008** *3*, 1171–1179.
55. Laskowski, R. A., MacArthur, M. W., Thornton, J. M. Validation of protein models derived from experiment. *Curr. Opin. Struct. Biol.* **1998** *8*, 631–639.
56. Potterton, L., McNicholas, S., Krissinel, E., Gruber, J., Cowtan, K., Emsley, P., Murshudov, G. N., Cohen, S., Perrakis, A., Noblec, M. Developments in the *CCP*4 molecular-graphics project. *Acta Crystallogr.* **2004** *60*, 2288–2294.
57. Shanks, E. J., Ong, H. B., Robinson, D. A., Thompson, S., Sienkiewicz, N., Fairlamb, A. H., Frearson, J. A. Development and validation of a cytochrome *c*-coupled assay for pteridine reductase 1 and dihydrofolate reductase. *Anal. Biochem.* **2010** *396*, 194–203.
58. Ferrari, S., Morandi, F., Motiejunas, D., Nerini, E., Henrich, S., Luciani, R., Venturelli, A., Lazzari, S., Calò, S., Gupta, S., Hannaert, V., Michels, P. A. M., Wade, R. C., Costi, M. P. Virtual screening identification of nonfolate compounds, including a CNS drug, as antiparasitic agents inhibiting pteridine reductase. *J. Med. Chem.* **2011** *54*, 211–221.
59. Tan, X., Huang, S., Ratnam, M., Thompson, P. D., Freisheim, J. H. The importance of loop region residues 40-46 in human dihydrofolate reductase as revealed by site-directed mutagenesis. *J. Biol. Chem.* **1990** *265*, 8027–8032.
60. Schrödinger, LLC, New York, NY, Schrödinger Release 2015-4, **2015**, LigPrep v3.6; Epik v3.4; Protein Preparation Wizard (PrepWizard); SiteMap v3.7; Glide v6.9; Induced Fit Docking Protocol, Prime v4.2.
61. Linciano, P., Dawson, A., Pöhner, I., Costa, D. M., Sá, M. S., Cordeiro-da-Silva, A., Luciani, R., Gul, S., Witt, G., Ellinger, B., Kuzikov, M., Gribbon, P., Reinshagen, J., Wolf, M., Behrens, B., Hannaert, V., Michels, P. A. M., Nerini, E., Pozzi, C., Di Pisa, F., Landi, G., Santarem, N., Ferrari, S., Saxena, P., Lazzari, S., Cannazza, G., Freitas-Junior, L. H., Moraes, C. B., Pascoalino, B. S., Alcântara, L. M., Bertolacini, C. P., Fontana, V., Wittig, U., Müller, W., Wade, R. C., Hunter, W. N., Mangani, S., Costantino, L., Costi, M. P. Exploiting the 2-Amino-1,3,4-thiadiazole scaffold to inhibit *Trypanosoma brucei* pteridine reductase in support of early-stage drug discovery. *ACS Omega* **2017** *2*, 5666–5683.
62. Shelley, J. C., Cholleti, A., Frye, L. L., Greenwood, J. R., Timlin, M. R., Uchimaya, M. Epik: a software program for pK_a prediction and protonation state generation for drug-like molecules. *J. Comput. Aided Mol. Des.* **2007** *21*, 681–691.

63. Greenwood, J. R., Calkins, D., Sullivan, A. P., Shelley, J. C. Towards the comprehensive, rapid, and accurate prediction of the favorable tautomeric states of drug-like molecules in aqueous solution. *J. Comput. Aided Mol. Des.* **2010** *24*, 591–604.
64. Sanschagrin, P. C., Kuhn, L. A. Cluster analysis of consensus water sites in thrombin and trypsin shows conservation between serine proteases and contributions to ligand specificity. *Protein Sci.* **1998** *7*, 2054–2064.
65. Sastry, G. M., Adzhigirey, M., Day, T., Annabhimoju, R., Sherman, W. Protein and ligand preparation: parameters, protocols, and influence on virtual screening enrichments. *J. Comput. Aided Mol. Des.* **2013** *27*, 221–234.
66. Li, H., Robertson, A. D., Jensen, J. H. Very fast empirical prediction and rationalization of protein pKa values. *Proteins* **2005** *61*, 704–721.
67. Banks, J. L., Beard, H. S., Cao, Y., Cho, A. E., Damm, W., Farid, R., Felts, A. K., Halgren, T. A., Mainz, D. T., Maple, J. R., Murphy, R., Philipp, D. M., Repasky, M. P., Zhang, L. Y., Berne, B. J., Friesner, R. A., Gallicchio, E., Levy, R. M. Integrated Modeling Program, Applied Chemical Theory (IMPACT). *J. Comput. Chem.* **2005** *26*, 1752–1780.
68. Halgren, T. New method for fast and accurate binding-site identification and analysis. *Chem. Biol. Drug Des.* **2007** *69*, 146–148.
69. Halgren, T. A. Identifying and characterizing binding sites and assessing druggability. *J. Chem. Inf. Model.* **2009** *49*, 377–389.
70. Friesner, R. A., Banks, J. L., Murphy, R. B., Halgren, T. A., Klicic, J. J., Mainz, D. T., Repasky, M. P., Knoll, E. H., Shelley, M., Perry, J. K., Shaw, D. E., Francis, P., Shenkin, P. S. Glide: a new approach for rapid, accurate docking and scoring. 1. Method and assessment of docking accuracy. *J. Med. Chem.* **2004** *47*, 1739–1749.
71. Halgren, T. A., Murphy, R. B., Friesner, R. A., Beard, H. S., Frye, L. L., Pollard, W. T., Banks, J. L. Glide: a new approach for rapid, accurate docking and scoring. 2. Enrichment factors in database screening. *J. Med. Chem.* **2004** *47*, 1750–1759.
72. Friesner, R. A., Murphy, R. B., Repasky, M. P., Frye, L. L., Greenwood, J. R., Halgren, T. A., Sanschagrin, P. C., Mainz, D. T. Extra Precision Glide: Docking and scoring incorporating a model of hydrophobic wnclosure for protein-ligand complexes. *J. Med. Chem.* **2006** *49*, 6177–6196.
73. Sherman, W., Beard, H. S., Farid, R. Use of an induced fit receptor structure in virtual screening. *Chem. Biol. Drug Des.* **2006** *67*, 83–84.
74. Sherman, W., Day, T., Jacobson, M. P., Friesner, R. A., Farid, R. Novel procedure for modeling ligand/receptor induced fit effects. *J. Med. Chem.* **2006** *49*, 534–553.
75. Jacobson, M. P., Pincus, D. L., Rapp, C. S., Day, T. J. F., Honig, B., Shaw, D. E., Friesner, R. A. A hierarchical approach to all-atom protein loop prediction. *Proteins* **2004** *55*, 351–367.
76. Jacobson, M. P., Friesner, R. A., Xiang, Z., Honig, B. On the role of the crystal environment in determining protein side-chain conformations. *J. Mol. Biol.* **2002** *320*, 597–608.
77. Lagorce, D., Sperandio, O., Baell, J. B., Miteva, M. A., Villoutreix, B. O. FAF-Drugs3: a web server for compound property calculation and chemical library design. *Nucleic Acids Res.* **2015** *43*, W200–207. https://fafdrugs4.mti.univ-paris-diderot.fr (accessed October 2020).
78. Bowling, T., Mercer, L., Don, R., Jacobs, R., Nare, B. Application of a resazurin-based high-throughput screening assay for the identification and progression of new treatments for human African trypanosomiasis. *Int. J. Parasitol. Drugs Drug Resist.* **2012** *2*, 262–270.
79. Sereno, D., Cavaleyra, M., Zemzoumi, K., Maquaire, S., Ouaissi, A., Lemesre, J. L. Axenically grown amastigotes of *Leishmania infantum* used as an in vitro model to investigate the pentavalent antimony mode of action. *Antimicrob. Agents Chemother.* **1998** *42*, 3097–3102.